Characterization of Heterodimer of Cr_7Mn Using Custom Loop Gap Resonators

Peter Jones

August 25, 2025

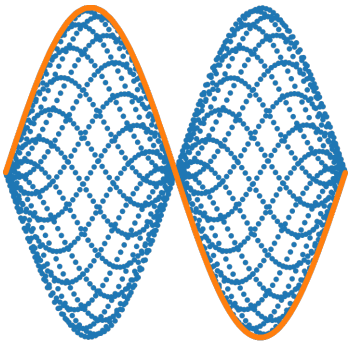

Collett Lab

Advised By:
Professor Charles Collett

Abstract

Quantum Computing has received significant attention over the last 25 years due to its potential advantages over classical computing. Molecular Nanomagnets (MNMs) have showed promise as qubits due to their chemical engineerability. Our lab works with the two variants of the MNM Cr_7Mn with two separate transition frequencies between low energy states. When coupled together these variants form a heterodimer. We provide an initial characterization of the high frequency variant as well as the heterodimer. We design custom built Loop Gap Resonators for use in Electron Spin Resonance to probe our system. Initial measurements for T_1, T_2 and field dependence are found. These measurements allow for a baseline for measuring coupling strength of the heterodimer.

Contents

List of Figures

1 Introduction

Quantum Computing (QC) is the quantum mechanical analog to classical computing. A bit, the basic unit of information in classical computing, is replaced by the qubit, the basic unit of information for Quantum Computing. QC represents potential advantages over classical computing due to qubits' properties of superposition and entanglement allowing for significantly higher computational power across select fields. Potential applications of QC include simulations of natural phenomena, factorization of large numbers, drug development and machine learning [6]. Several materials have been investigated as potential qubits, with molecular nanomagnets showing promising early results. Molecular nanomagnets (MNMs) are spin systems which can be chemically engineered to have properties desirable of qubits [7].

In our research, we work with electron spins within MNMs to demonstrate their viability as qubits. We manipulate our qubits using Electron Spin Resonance (ESR) to better understand how they might be used in eventual quantum gate operations. Multi-qubit gate operations used in full-scale QC requires two qubits being coupled together. We achieve this using a heterodimer sample with two different spin systems (monomers) coupled together, allowing us to take advantage of both superposition and entanglement in our qubits. To understand and exploit this coupling, we can manipulate and probe our spin systems with radiofrequency (RF) pulses using ESR. Previous work has focused on manipulating and characterizing a monomer with a lower transition frequency between low energy states, but precise measurements of a higher frequency variant, and inter-spin coupling, are still lacking.

My thesis aims to begin to understand how our heterodimer system behaves. Our eventual goal is to be able to interact with both spin systems in a heterodimer simultaneously. A first step is to have a baseline for how our individual monomers behave without any coupling. A monomodal Loop Gap Resonator (LGR) is constructed to allow for ESR with our high frequency

monomer. Characterization of this monomer is conducted using this LGR. We also begin initial characterization of our heterodimer using monomodal resonators. A bimodal resonator is constructed with the goal of being able to probe a heterodimer sample which contains our coupled spin systems. Our research in this paper will serve as a guide for understanding the behavior of our two variants in our dimer system. This will in turn allow us to work towards measuring the coupling of our dimer system and eventually towards implementing multi-qubit gates.

2 Background

2.1 Quantum Computing

Quantum Computing (QC) continues to show promise as the next step in Quantum Information Processing and computational power. A principal application of the field is simulating purely quantum mechanical processes. The exploration of other natural processes, and the ability to apply Peter Shor's 1994 theoretical algorithm for factorization of large numbers, offer further motivation to demonstrate quantum computing capabilities experimentally [6]. While Quantum Computers will not replace classical computers or prove advantageous over them for all computations, they do represent a computational advantage in certain applications. This has driven a recent surge in resources and time dedicated to better understanding how large-scale QC might be possible – both in academia and the private and public sector.

Computational advantages for QC are due to it being governed by quantum mechanics, rather than classical mechanics. Due to superposition, we can encode more information in each qubit itself. The true power of QC comes in the combination of multiple qubits. Through quantum entanglement, we can have two qubits which are entangled, meaning that the state of one of the qubits depends on the state of the other qubit. This contrasts

with classical computation where bits are independent of each other. As we increase the number of qubits in a system, the power of superposition and entanglement combine to compound our computational power. Specifically, for a quantum system with N qubits, 2^{N-1} bits of information can be stored, while in a classical system only N bits of information could be stored [8].

Quantum Computing continues to be studied given the above benefits over classical computing, but there are limitations to existing systems. Our work seeks to better understand the systems we employ as qubits to help combat some of these problems. Issues currently facing QC include the difficulty in scaling to a large enough number of qubits to potentially simulate real quantum systems. Limitations in coherence time, the time during which a quantum state stays quantum before collapsing to an unknown state on interactions with its environment, and an understanding of entanglement between qubits are two key areas which continue to be explored [8].

2.2 Molecular Nanomagnets as Qubits

A promising class of materials being investigated as qubits are molecular nanomagnets (MNMs). MNM's are molecules which are chemically engineered to contain one or more spins interacting in a way which we can utilize for quantum information processing. MNMs individually contain a collection of strongly interacting spins surrounded by ligands so each molecule can be modeled as an individual spin using the giant spin approximation [9].

Significant work is currently being done on MNMs as qubits. Importantly, recent work has shown that their engineerability makes it possible to have readily accessible low energy states from which qubits can be constructed. These systems have also been demonstrated to have the potential of increasing coherence times to a level needed for large scale quantum gate operations, though achieving this level of coherence still remains a challenge [7].

Quantum Computing requires both single and multi-qubit gates. Monomers of MNMs are useful as single qubits, but two coupled spin systems forming

a heterodimer system would allow for multi-qubit gate operations. The coupling between these spin systems can be chemically engineered [1]. The heterodimer can be constructed to allow both spin systems to operate at clock transitions, enhancing the coherence time of the overall system [10]. My thesis will design two loop gap resonators which can be used to probe both variants of our heterodimer simultaneously and independently. We then begin characterization of our high frequency monomer and our heterodimer. This lays the groundwork for measuring the coupling strength in our heterodimer.

3 Theory

3.1 Cr_7Mn

Heterodimers which would eventually be used in quantum gate operations are formed by coupling two variants of the same monomer. This monomer is formed by substituting an $S = 5/2$ Mn^{2+} into a ring of 8 Cr^{3+} $S = 3/2$, forming the molecule Cr_7Mn, shown in Figure 1 [1].

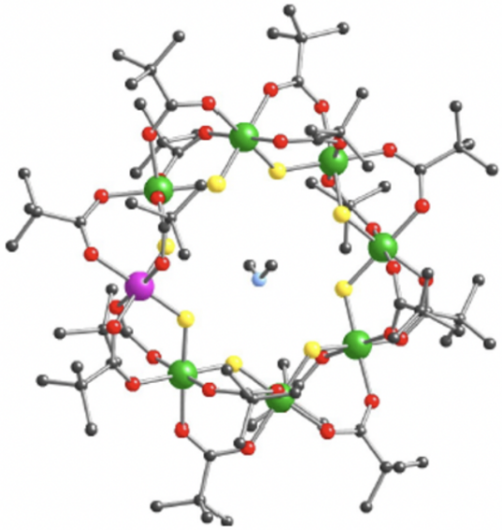

Figure 1: Cr_7Mn molecular structure. Shown are 7 Cr^{3+} ions (green) and Mn^{2+} ion (purple) [1]

We use two variants of this monomer. The first is a low frequency variant, $[Pr_2NH_2][Cr_7MnF_8(Piv)_{15}(O_2C-py)]$ [2] which has already been well characterized. The second is a higher frequency variant. Our high frequency variant is $\{[Cr_7MnF_3(EtgLu)(Piv)_{15}(O_2C-Py)]\}$ [11]. In the first portion of our research we are working primarily with the high frequency variant.

This system can be modeled as an $S = 1$ system. Two of the energy eigenstates of this spin system form the qubit which is the basis for potential quantum logic gate operations.

Given that this is an $S = 1$ system, we can use the standard spin operators $\hat{S}_x$, $\hat{S}_y$ and $\hat{S}_z$ to work with our system. The high frequency variant of Cr_7Mn can be described by the Hamiltonian:

$$\hat{H} = -D\hat{S}_z^2 + E(\hat{S}_x^2 - \hat{S}_y^2) - g\mu_B \mathbf{B} \cdot \mathbf{S} \text{ [1]} \tag{1}$$

in which $D = 16.5$ GHz, $E = 2.6$ GHz, g is the Landè g-factor of 1.96,

and μ_B is the Bohr magneton [10]. These values are found from high field and frequency spectroscopy being fit to low field. Further research is being done to confirm them experimentally. For the low frequency variant, we have $D = 21$ GHz and $E = 1.9$ GHz. This Hamiltonian describes a three eigenstate system, shown in Figure 2.

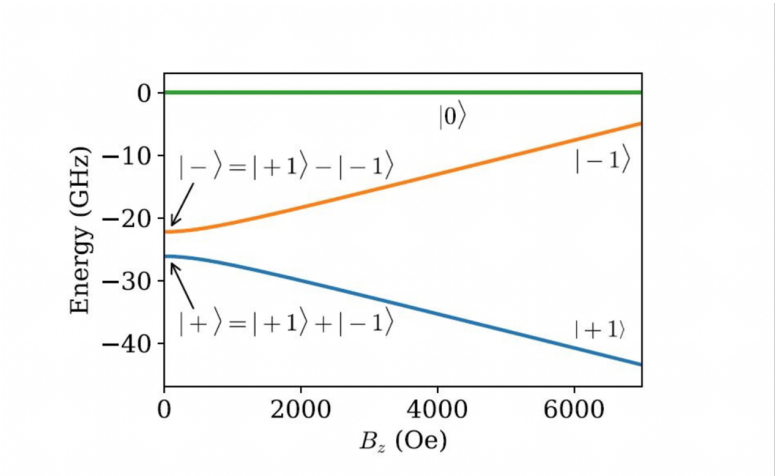

Figure 2: Energy Levels for Cr_7Mn Monomer. Note that at 0-field we have a superposition of the $|+1\rangle$ and $|-1\rangle$ states forming the $|-\rangle$ and $|+\rangle$ states, while at high field $|+1\rangle$ and $|-1\rangle$ are energy eigenstates Also note that since source was published the labels for $|+\rangle$ and $|-\rangle$ states have been flipped [1]

These energy levels can be described using our energy eigenstates in the $\hat{S}_z$ basis, that is, the set of unit vectors with which we describe the entirety of the state. The $\hat{S}_z$ eigenbasis can be expressed:

$$|+1\rangle = \begin{bmatrix} 1 \\ 0 \\ 0 \end{bmatrix}, \; |-1\rangle = \begin{bmatrix} 0 \\ 0 \\ 1 \end{bmatrix}, \; |0\rangle = \begin{bmatrix} 0 \\ 1 \\ 0 \end{bmatrix} \tag{2}$$

From the Zeeman effect, we note that at high field our eigenstates are well established and have distinct splitting. However, at 0 field, the transverse anisotropy term (the second term in equation 1) mixes the two low-energy $\hat{S}_z$

states in Figure 2, thereby breaking the zero field degeneracy of the states [1]. This leads to the superposition of these states at 0 field, whose states can better be described at zero field by:

$$|\pm\rangle = \frac{1}{\sqrt{2}}[|+1\rangle \pm |-1\rangle] \tag{3}$$

At 0 field, we thus have the eigenstates given in the $\hat{S_z}$ eigenbasis by:

$$|+\rangle = \frac{1}{\sqrt{2}} \begin{bmatrix} 1 \\ 0 \\ 0 \end{bmatrix} + \frac{1}{\sqrt{2}} \begin{bmatrix} 0 \\ 0 \\ 1 \end{bmatrix} \tag{4}$$

$$|-\rangle = \frac{1}{\sqrt{2}} \begin{bmatrix} 1 \\ 0 \\ 0 \end{bmatrix} - \frac{1}{\sqrt{2}} \begin{bmatrix} 0 \\ 0 \\ 1 \end{bmatrix} \tag{5}$$

$$|0\rangle = \begin{bmatrix} 0 \\ 1 \\ 0 \end{bmatrix} \tag{6}$$

Cr_7Mn is a 3-state system, but for quantum gate operations we need to use qubits within a two-state system (and eventually pairs of qubits in an effective four state system). For our purposes we are only concerned with the two lowest states at zero field: $|+\rangle$ and $|-\rangle$.

3.2 Heterodimer

Coupling our two variants of Cr_7Mn gives rise to our heterodimer system. Specifically, $[Pr_2NH2][Cr_7MnF_8(Piv)_15(O_2C-py)][Cr_7MnF_3(Etglu)(piv)_{15}]$ [2], similar to the dimer shown in Figure 3.

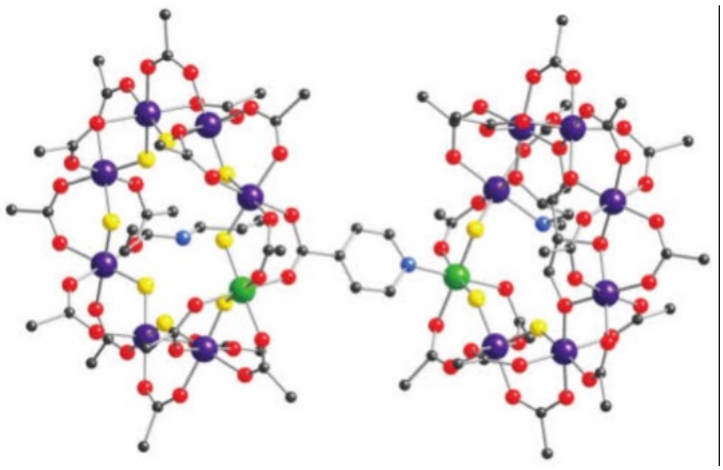

Figure 3: Dimer Molecular Structure. Dimer above is for a Cr_7Ni system, which has similar structure to our Cr_7Mn dimer [2].

Our dimer system can be described by combining the two Hamiltonians of our individual spin systems, along with an additional term describing the coupling between the two spins. This gives rise to our new Hamiltonian for this system at zero field:

$$\hat{H} = \hat{H}_1 + \hat{H}_2 + \hat{H}_J \text{ [10]} \tag{7}$$

where $\hat{H}_1$, $\hat{H}_2$ describe the two individual spin systems, and $\hat{H}_J$ is the coupling term [10]. This new Hamiltonian describes a system with nine energy eigenstates. We are interested in the lowest four states given their clock transitions, shown in Figure 4. Note that at zero field we have no field dependence to first order, evidence of clock transitions being preserved in the dimer.

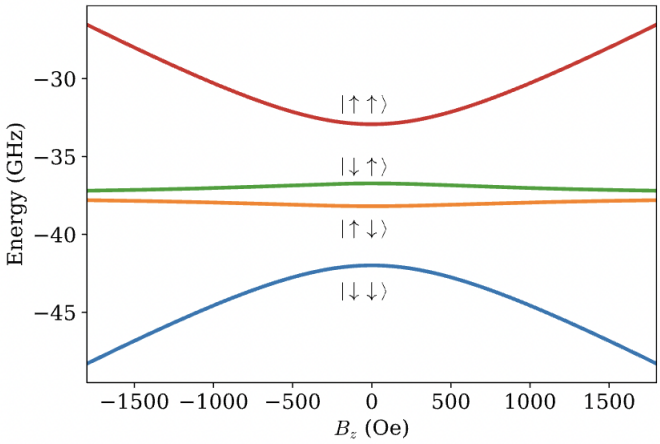

Figure 4: Cr_7Mn dimer four lowest energy eigenstates. Note the limited dependence on field to first order at 0 field, evidence of a clock transition [3].

We can redefine our $\hat{H}_J$ term in equation (7) in terms of our two spin systems and our coupling between the two. To do this, we consider our interaction between our two spin systems as a bilinear exchange interaction [10]. Knowing this, our $\hat{H}_J$ term can be described as [10]:

$$\hat{H}_J = \hat{\vec{S}}_1 \cdot J \cdot \hat{\vec{S}}_2 \tag{8}$$

Here, we have $\hat{\vec{S}}_1 = \hat{S}_{x_1}\mathbf{x} + \hat{S}_{y_1}\mathbf{y} + \hat{S}_{z_1}\mathbf{z}$ describing our spin system of the first qubit, $\hat{\vec{S}}_2 = \hat{S}_{x_2}\mathbf{x} + \hat{S}_{y_2}\mathbf{y} + \hat{S}_{z_2}\mathbf{z}$ the spin system of the second qubit, and J our coupling between the two. J depends not only on the chemical strength of the link between our two systems in the dimer, but also on the physical distance between our two systems and their individual magnetic moments [12]. As of now, there have been no precise measurements of J. We hope to accomplish this using Double Electron Electron Resonance (DEER), discussed further in section 3.9.

3.3 Clock Transitions

Quantum gate operations require qubits with long coherence times. Coherence will be addressed more in section 3.5. A significant improvement in coherence times can be achieved by operating at clock transitions [10]. Clock transitions, whose name comes from their use in atomic clocks, are found at regions where the energy difference between states has zero dependence to first order on magnetic fields [13]. Put another way, clock transitions are highly insensitive to local field fluctuations – allowing for longer coherence (though decoherence still occurs from other factors). We can identify clock transitions as regions where energy as a function of field has a 1st derivative of zero. In Figure 2 and Figure 4, we see this occurring at zero field. We want to operate at zero field to minimize decoherence and drive more stable transitions.

3.4 Electron Spin Resonance

The main technique we use to interact with our spin system is Electron Spin Resonance (ESR). Our system is an $S = 1$ system, but since we are only looking at the lowest two states we can treat it as an effective spin $\frac{1}{2}$ system. For a generic spin $\frac{1}{2}$ system, we have eigenstates in the $\hat{S}_z$ basis:

$$|+\rangle = \begin{bmatrix} 1 \\ 0 \end{bmatrix}, |-\rangle = \begin{bmatrix} 0 \\ 1 \end{bmatrix} \tag{9}$$

We can write the spin system more generally as a superposition of these two states:

$$|\psi\rangle = \alpha|+\rangle + \beta|-\rangle \tag{10}$$

This superposition can be visualized as a unique vector in 3-dimensional space. The tip of this vector can trace any point along a unit sphere – which is referred to as the Bloch Sphere. Consider the case that our spin system

starts initially pointing directly upwards on the Bloch Sphere, in the $|+\rangle$ state, aligned with the z-axis. This is shown in Figure 5.

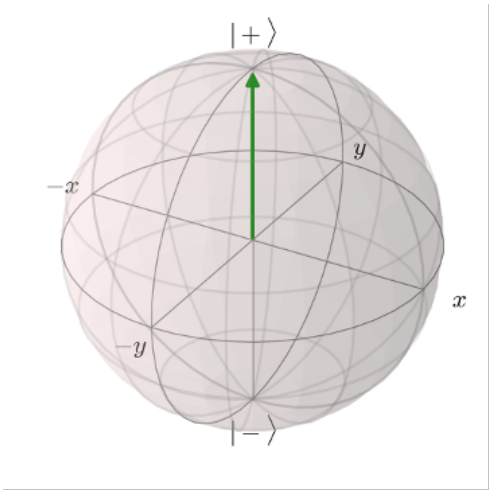

Figure 5: Bloch Sphere shown with Spin in $|+\rangle$ state.

By applying an oscillating field in the form of an RF excitation pulse, we can effectively "tip" our spin system. Now our spin system has been moved off our z-axis by some angle ϕ to some state $|\psi\rangle$. Depending on the power or length of the RF pulse which we apply, we can tip our spins by varying amounts – allowing for us to move to various points on the Bloch Sphere and from one energy level to the other. This tip angle can be theoretically given by:

$$\phi = \gamma B_1 t \tag{11}$$

where γ is the gyromagnetic ratio, B_1 the applied field strength, and t the pulse time [14]. The tip of our spin vector can then trace any point along our Bloch Sphere. A depiction of a few of these potential positions are shown in Figure 6, with tip angles 0, 30, 60 and 90 degrees from $|+\rangle$ to the x axis.

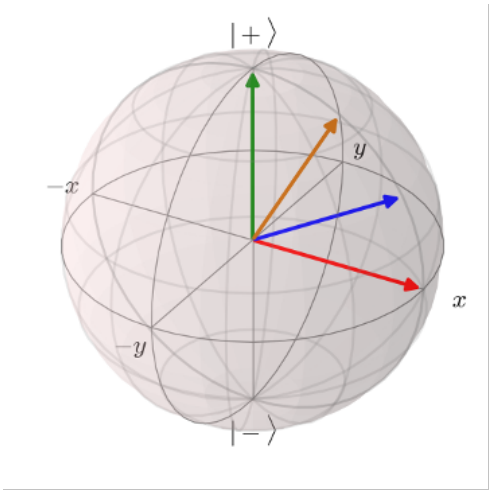

Figure 6: Bloch Sphere with net spins in a variety of superpositions of $|+\rangle$ and $|-\rangle$ states.

Now we know how to manipulate an individual spin from one state to another or place it in a superposition of states. We need to have a practical way to manipulate and measure our spins. In our sample, we are dealing with a collection of 10^{16} different spin systems [11]. When tipped, our spins will precess around the intrinsic anisotropy axis aligned with our $|+\rangle$ on the Bloch Sphere. This precession leads to an oscillating field produced by the spins, inducing currents in the resonator which can be read out as a voltage or EMF, generating a signal. Individual EMFs are far too weak for us to read out any signal, but the collection of spins, if all pointed in the same direction along the Bloch Sphere, produces an EMF strong enough for us to read.

3.5 Loop Gap Resonators

These pulse sequences are only possible if we can generate a transverse oscillating field and read out any corresponding signal from the spins. Transverse oscillating field pulses are created using custom made Loop Gap Res-

onators (LGRs). An LGR can be designed to operate at one (monomodal), two (bimodal), or more (multimodal) resonant frequencies. Their basic design features a capacitive gap with an inductive loop fixed at one end, as shown in Figure 7.

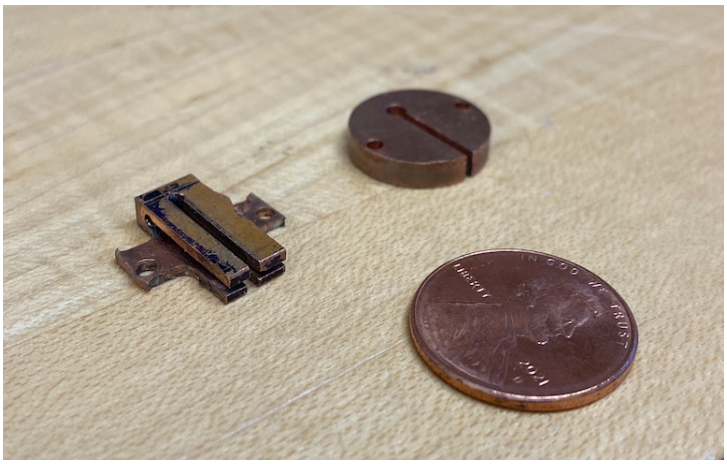

Figure 7: A traditional monomodal LGR (top right) and a bimodal LGR (bottom left) next to a penny for relative size comparison.

The LGR can be modeled as a lumped RLC circuit with spatially separated electric and magnetic fields. An electric field is present between the two walls of the gap which act as capacitor plates, while the loop acts as an inductor with a magnetic field concentrated at the center of the loop. For a generic LGR, the inductance and capacitance are given by:

$$L = \frac{\mu_0 \pi r^2}{z + 0.9r} \tag{12}$$

$$C = \epsilon_r \epsilon_0 \frac{(w+t)(z+t)}{nt} \tag{13}$$

where w is the width of the gap, n is the number of gaps, z the combined length of the loop and gap, t the thickness of gaps, ϵ_r the dielectric constant, μ_0 the permeability of free space, and ϵ_0 the permittivity of free space [15].

The resonant frequency is given by:

$$f_0 = \frac{1}{2\pi\sqrt{LC}} \tag{14}$$

We can measure how efficiently the resonator stores and releases energy using the quality factor, Q, given by:

$$Q = \frac{f_c}{\Delta f} \text{ [15]} \tag{15}$$

where f_c is the resonant frequency of the resonator and Δf the bandwidth of the resonance. Alternatively, we can extract Q from the ring down of our resonator - how long our resonator radiates energy after it receives a pulse. The loss of energy goes as an exponential decay, with our time t for decay given by [3]:

$$t_{decay} = \frac{Q}{\pi f_c} \tag{16}$$

A higher Q results in a longer ring down of the signal, and is often less desirable for pulsed ESR experiments when interacting with a short T_2 timescale. A lower Q enables rapid pulse sequences to be applied without any signal being swamped by the resonator ring down.

LGRs feature a high filling factor compared to other resonator designs. Filling factor measures the ratio of sample volume to mode volume [15]. Mode volume is the volume where the magnetic field is highly concentrated [16]. A higher filling factor means more of our mode volume is filled by the sample, allowing for stronger interactions between our sample and the field. Due to their customizability, relatively low Q, and high filling factor, LGRs are ideal for ESR experiments when operating below X-band frequencies, typically defined as 8-12 GHz [17]. The resonant frequency of an LGR can be tuned by introducing a dielectric into the gap(s). While each LGR has an intrinsic Q, the effective Q can be tuned by changing the coupling of the LGR with

a capacitively or inductively coupled antenna used to provide RF excitation pulses into the resonator. In our experiments, we principally deal with our antenna operating in reflection mode, meaning that it is responsible for both exciting our LGR and reading out any response signal as well [3].

3.6 Coherence

In section 3.3, we made an assumption that when we tip an ensemble of spins, all spins precess at the same rate. This is not the case. Suppose we tip an ensemble of spins such that they are oriented along the x-axis on our Bloch Sphere. These spins will precess around our z-axis, with some precessing faster than others. This difference is due to inhomogeneities in local field and molecules experiencing slightly different Hamiltonians leading to differences in energy splitting 2E between the $|+\rangle$ and $|-\rangle$ states [8]. To an observer in the reference frame of a spin (say on the x-axis), it will appear as though spins are spreading away from the x-axis. This process is called dephasing. We can mitigate this effect. Suppose that as our spins spread out we apply a pulse which rotates our spins 180 degrees about the y axis. This pulse inverts the direction of precession for the spins, causing those precessing faster to now have to "catch up" to those precessing slower. At some time later, the spins are again in phase for a brief period. We will refer to this process as "refocusing". It will be described further in section 3.7.

Refocusing allows us to partially mitigate dephasing effects. However, up until this point we have assumed that individual spins precess at the same rate throughout time. This is not the case. Individual differences in local field and energy splitting are not static, but fluctuating with time [8]. This makes our technique for refocusing our spins less effective. Over time, our spins will precess at different rates than they did at some time prior. Given enough time, the spins will dephase even with refocusing. This process is called decoherence and has the effect of the spin system moving from a known quantum state to a random quantum state over time.

Coherence time is characterized by T_2, the spin-spin relaxation time for our system, which will be discussed more in section 3.7. T_2 has been shown to improve by minimizing dipolar interactions between spins through dilution in a non-magnetic solvent [18]. Decoherence can also be improved through limiting the effect of fluctuations in local fields by operating at clock transitions, as discussed in section 3.2. Operating at low temperatures limits thermal effects on coherence time by also limiting dipolar interactions as spins increasingly stay at lower energy states and experience fewer thermal excitations [8]. Our apparatus supports operation at 3 K indefinitely and 1.5 K for short periods, increasing our T_2 enough to measure.

3.7 Cr_7Mn at Low Temperature

Given operation at low temperature to limit decoherence, we need to understand our spin 1 system's population distribution amongst our three states at these temperatures. Consider our zero-field Hamiltonian:

$$\hat{H} = -D\hat{S}_z^2 + E(\hat{S}_x^2 - \hat{S}_y^2) \tag{17}$$

The Hamiltonian operating on our Eigenstates yields:

$$\hat{H}|+\rangle = (-D + E)|+\rangle \tag{18}$$

$$\hat{H}|-\rangle = (-D - E)|+\rangle \tag{19}$$

$$\hat{H}|0\rangle = 0 \tag{20}$$

Giving energies of:

$$E_{|+\rangle} = -D + E \tag{21}$$

$$E_{|-\rangle} = -D - E \tag{22}$$

$$E_{|0\rangle} = 0 \tag{23}$$

Now consider our system at thermal equilibrium, described by the Boltzmann distribution:

$$P(S) = \frac{1}{Z} e^{\frac{-E(S)}{k_B T}} \tag{24}$$

Where our partition function Z is given by:

$$Z = \sum_{S} e^{\frac{-E(S)}{k_B T}} \tag{25}$$

Remembering that D = 16.5 GHz and E = 2.6 GHz, we use our eigenvalues from equations (21), (22) and (23) to calculate our energy levels. First, we calculate our probabilities at 3 K, our normal operating temperature:

$$P_{3K}(|+\rangle) = 0.346 \tag{26}$$

$$P_{3K}(|-\rangle) = 0.376 \tag{27}$$

$$P_{3K}(|0\rangle) = 0.277 \tag{28}$$

Now, let's calculate our probabilities for 1.5 K:

$$P_{1.5K}(|+\rangle) = 0.354 \tag{29}$$

$$P_{1.5K}(|-\rangle) = 0.419 \tag{30}$$

$$P_{1.5K}(|0\rangle) = 0.227 \tag{31}$$

At 1.5 K and 3 K, the system is less likely to occupy the $|0\rangle$ state than either of the lower energy states. However, at either temperature we still have a relatively high portion of spins in our excited state. If we could operate at temperatures of a dilution refrigerator [19], say 25 mK, we have:

$$P_{25mK}(|+\rangle) = 0.00005 \tag{32}$$

$$P_{25mK}(|-\rangle) = 0.99995 \tag{33}$$

$$P_{25mK}(|0\rangle) = 0 \tag{34}$$

At close to absolute zero our excited state population approaches zero. Given our operating temperatures, we can model our spin 1 system as a spin $\frac{1}{2}$ system focusing on the two lowest energy states.

3.8 Pulse Sequences

Taking our system to be an effective 2 state spin system, we use several pulse sequences to manipulate and characterize it. Figure 8a shows our system where the majority of spins are fully relaxed in the "up" state, aligned with the z-axis. Suppose we apply a 90 degree pulse, tipping our spins into the transverse plane, as shown in Figure 8b. At this point our spins undergo both longitudinal and transverse relaxation. Longitudinal relaxation, characterized by T_1, is the process by which our spins return from an exited state to the ground state shown in Figure 8a and is significantly slower than transverse relaxation. As individual spins tunnel from the excited state to the ground state, the average magnetization moves back to the position in 8a. Simultaneously, our system is dephasing through transverse relaxation, depicted in panel C. As described in section 3.5, this dephasing is due to impurities in individual spins axial anisotropies and energy splitting 2E. These variations are both static and time-varying. To combat the effects of static inhomogeneities, we refocus our spins as described in section 3.5. After some time τ, we tip our spins 180 degrees in the transverse plane, at which point they begin to refocus. This process is shown from panels D to E. After some additional time τ, our spins are again in phase. This produces an EMF which can be picked up by our antenna. This signal is our echo, and the sequence a Hahn echo sequence.

Due to our time-varying inhomogeneities, as we increase τ, our echo weakens. As τ grows, our 180 degree refocusing pulse is no longer effective at refocusing our transverse magnetization as spins experience fluctuating inho-

mogeneities rather than static inhomogeneities. Our signal is thus a function of delay time, 2τ. We measure our T_2 by fitting an exponential decay to this relationship.

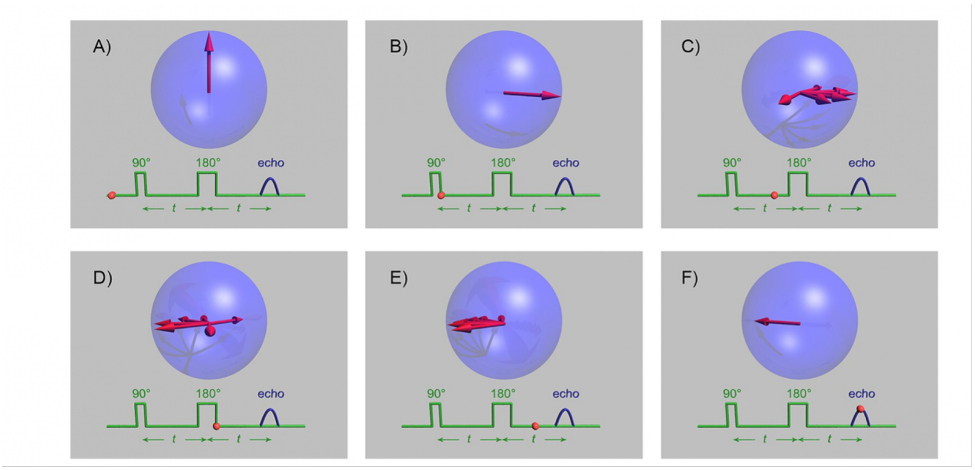

Figure 8: Cartoon Depiction of Hahn echo Sequence as Pulses and Resultant Spin Positions on Bloch Sphere. (A) shows spin at rest in "up" position. (B) shows spin after a 90 degree tip. (C) shows dephasing process in transverse plane. (D) shows a 180 degree tip in transverse plane. (E) shows refocusing process. (F) shows refocused spins again in phase producing echo [4].

To implement a Hahn echo sequence, we need to know how long a pulse must be to tip our spins by 90 or 180 degrees. An initial estimate for an appropriate pulse length can be found by guessing initial values and then varying our pulse lengths until a strong EMF is produced, after which we can perform more rigorous experiments to tune our pulse width.

By applying an initial nutation pulse before a Hahn echo, we can tip our spins by some angle ϕ. We set a constant delay time between this initial pulse and our Hahn echo pulses, somewhere between our expected T_1 and T_2. Changing the pulse length of the nutation pulse changes the angle ϕ which we are initially rotating our spins. This causes our echo signal to oscillate sinusoidally with varying nutation pulse lengths. Suppose for example our

nutation pulse tips our spins 90 degrees. A Hahn echo from this initial state will result in zero signal. This can be extrapolated to various tip angles leading to our echo signal oscillating. In this way we can find a 90 degree pulse where our signal is minimized. Our apparatus allows us to change from a 90 to 180 degree pulse by manipulating the field strength of the pulse using an attenuator, rather than the width of the pulse [3].

Applying a nutation pulse which inverts our longitudinal magnetization, we can recover our spin-lattice relaxation time T_1. Consider a nutation pulse which tips our spins 180 degrees, as shown in Figure 9a. If left undisturbed, our spin system will begin to relax back to thermal equilibrium. At some time α after our initial pulse, we apply a Hahn echo sequence. That is, we tip our spins 90 degrees, then refocus to create an echo. For a short α, this signal will be strong. Since our spins have not relaxed far off of the -z-axis, a 90 degree pulse will tip them into the transverse plane where an echo is produced. As α increases our net magnetization moves closer to our transverse plane. At this point, a 90 degree pulse would simply invert our net spin back to its original position in Figure 9a - where we would find no signal. Eventually, our net longitudinal magnetization would return to equilibrium, where a Hahn echo sequence would produce a strong signal, shown in Figure 9d. This process produces an exponential growth curve for signal as a function of α, which can be used to extract our T_1. Note that in our experiments, we set α to a non-zero starting time, thereby only fitting to positive echo signals at the steepest portion of our curve.

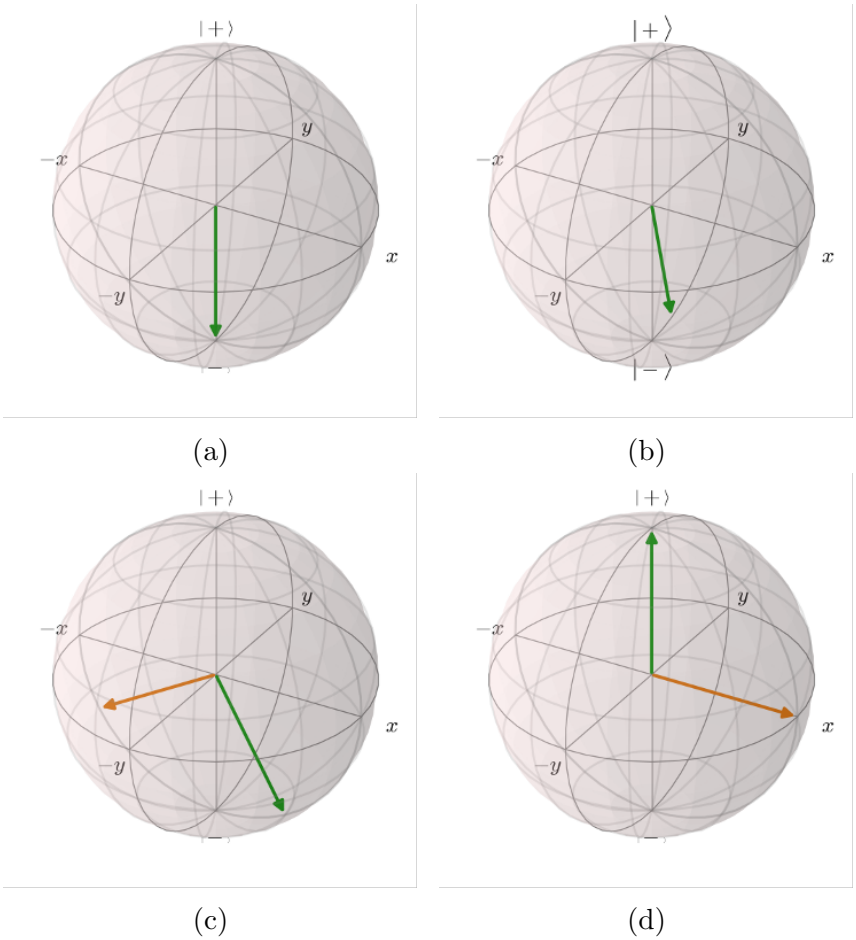

Figure 9: Inversion recovery sweep processes. (a) shows inverted spin. (b) shows recovering spin after some time α. (c) shows a 90 degree pulse (orange) applied after some recovery (green). (d) shows full signal recovery after total relaxation with 90 degree pulse (orange) in transverse plane.

3.9 Double Electron Electron Resonance

The above sequences are all applicable for single qubit manipulations, and will be helpful for any sort of phase or rotation gates [12]. However, in order to have any sort of functional CNOT or other multi-quibit gate schemes, we need to be able to experimentally measure the coupling described in Section

3.2. Double Electron Electron Resonance allows us to accomplish this.

DEER is accomplished by applying two different pulse sequences to each of our coupled spin systems simultaneously. We need a bimodal LGR to apply these pulses. This section will lay out the basic pulse sequences of DEER, but a detailed explanation of how to extract coupling information from the data is beyond the scope of this thesis.

To begin, we apply a standard Hahn echo sequence to one of our spin systems, which we will call our first spin. As shown above in Figure 8, an initial 90 degree pulse will tip our spins. We allow them to dephase for some time, which we will now call τ_1. A 180 degree pulse refocuses our spins and produces an echo. Given more time, our spins again dephase. A variable time T later, a 180 degree pulse is applied to our second spin system, as shown in Figure 10. For two uncoupled spins, the inversion of the second spin would have no impact on the precession rate of our first spin system. However, if the spins are coupled, our first spin's precession rate changes. Some time τ_2 after the first spins echo, a second refocusing pulse is applied, which then produces a second echo an additional τ_2 after.

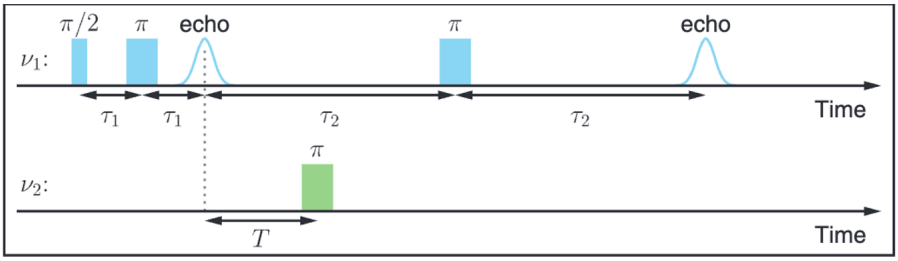

Figure 10: Pulse sequences for DEER. Top line depicts pulse sequence for target spin system and bottom line secondary spin system. Two sequences happen simultaneously using bimodal resonator [5].

By changing our time T between the initial echo and the 180 degree pulse on our secondary spin system we can manipulate the amplitude of the echo. This relationship roduces a sinusoidal variation in echo strength. The

frequency of these oscillations can be used to measure our systems coupling strength [20].

4 Apparatus

4.1 Cryostat Chamber

As described in section 3.5, for our systems it is advantageous to work at low temperatures. To do so, all experiments are performed in a cryostat made by Lake Shore Cryotronics, shown in Figure 11.

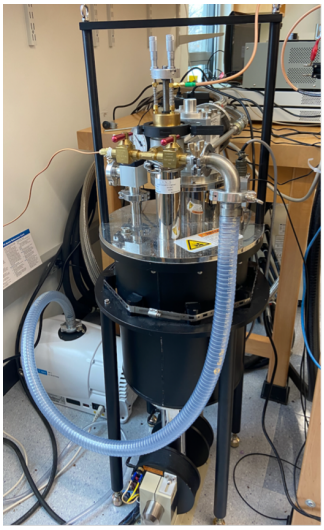

Figure 11: Cryostat

The cryostat can operate for an extended period at just above 3 K under normal conditions. The cryostat sample chamber can be cooled to just under 1.5 K for roughly five hours at a time by condensing helium within the sample chamber and then pumping the helium.

4.2 Sample Probes

Our setup consists of an LGR set inside a copper shield as shown in Figure 12. The shield helps to contain microwave radiation. Without the shield, our LGR would be a dipole radiator [15]. The shield is enclosed with a cap (not shown).

Figure 12: A prior monomodal Loop Gap Resonator shown sitting on washers inside of copper shield.

Two coaxial cables enter the shield through the top cap to act as antennas. These antennas carry RF pulses down from our spectrometer to the LGR. The antennas have had the outer piece of the coax stripped off, exposing the inner conductive section. This antenna can be positioned to capacitively or inductively couple to the LGR, as shown in Figure 13. For capacitive orientation, our antenna is bent to a right angle. For inductive, the antenna is formed into a loop and soldered to the outer portion of our coax. A third probe can be used to move a dielectric into the LGR gap using a G10 rod running through the cap of the shield [21].

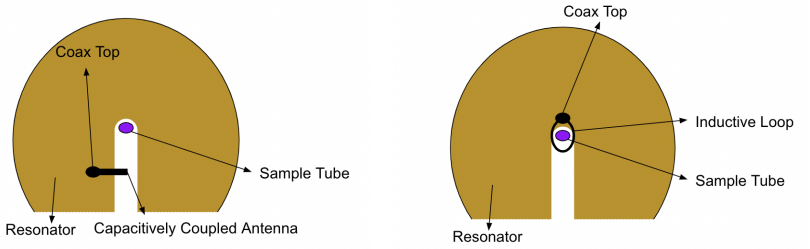

(a) (b)

Figure 13: Top view of capacitive (a) and inductive (b) coupling orientations for coaxial cable acting as antenna. Sample Tube also shown for reference.

A principle way to tune the resonant frequency and Q of an LGR is through changing the coupling strength of an antenna by changing its position relative to the resonator. In addition to tuning the coupling strength at room temperature, it is also advantageous to be able to adjust while the sample is cold. A sample probe shown in Figure 14 allows for this. The two antennas and G10 rod are attached to three individual micrometers, which enable for coupling strength to be tuned and a dielectric inserted while the sample is in the cryostat [21].

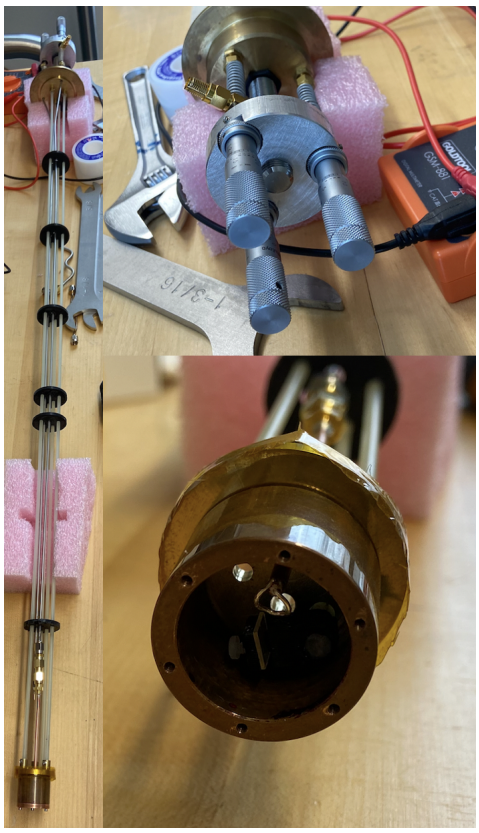

Figure 14: Adjustable sample probe. Shown with entire apparatus (left), shield with inductive loop inside (bottom right), and micrometer adjustments (top right).

4.3 Spectrometer

Our goal is to characterize how our sample behaves when probed with a variety of pulse sequences. To accomplish this, we need a way to send pulses down through our antennas into our LGR and read back responses as they come up. A homemade spectrometer generates pulses and detects responses. See [3] for further detail.

A Vector Network Analyzer (VNA) provides a more expedited on-bench measurement process to determine coupling strength and resonance. A CW

signal is sent into our resonator, with the reflected response being read out by the VNA. The VNA is principally used for measuring in-situ adjustments to our coupling using our sample probe. Once a reasonable coupling is established, all experiments are run using the spectrometer.

4.4 Background Subtraction

Our spectrometer generates pulses and reads back any responses, but this information is only as useful as it is distinguishable from noise. In an ideal world, a typical Hahn echo sequence would produce an echo which is easily visible relative to any background or static noise. The echo which we produce, even with an ideal pulse sequence maximizing amplitude, can still be swamped by noise, especially as we increase dilution levels and reduce the number of spins we interact with. One way we combat this is through averaging. By running the same sequence a number of times (often 10,000 or more), and then averaging out our resultant echo we are able to eliminate some noise. However, averaging does not help remove any systematic background such as ringdown from our resonator. To remove this background while amplifying our signal above the noise level we need another technique.

A solution to this problem is background subtraction through phase cycling. We apply four different pulse sequences for each of our desired sequence, a Hahn echo sequence. Each of these pulse sequences consists of a first pulse, to tip the spin 90 degrees, and a second pulse, to invert the spin 180 degrees, with differing relative phases between each of the four first pulses, and each of the four second pulses. For these pulses, we can define that a phase of 0 corresponds to the field pointing along the +y axis on our Bloch Sphere in Figure 15. A phase of π will then be along the -y axis, and so on. In our first sequence, the first pulse will have no relative phase, and the second pulse $\frac{\pi}{2}$. The second sequence will have its first pulse with a relative phase of π, with the second having a phase of $\frac{\pi}{2}$. The third sequence will have another π and $\frac{3\pi}{2}$ relative phase on the first and second pulses, respectively.

Finally, the last sequence has no phase on the first and another $\frac{3\pi}{2}$ phase on the second pulse.

Let's consider what these pulse sequences do to our spins on the Bloch Sphere. First we will look at the behavior of our four first pulses with different phase, which tip our spins by 90 degrees. As stated above, 0 phase applies a field along the +y axis, tipping our spins into the transverse plane on our Bloch Sphere along the +x axis, as shown in Figure 15 [22]. We define our +x axis such that any echo which we produce given this initial pulse phase of π, will have a positive signal. Given our pulse sequences, we will always have a 180 degree pulse which is a $\frac{\pi}{2}$ phase difference from our 90 degree pulse phase. This ensures that our transverse magnetization is always about either our +x or -x axis, leading to no change in the initial echo sign set by our 90 degree pulse phase. Therefore, our first and last sequences described above have a positive echo.

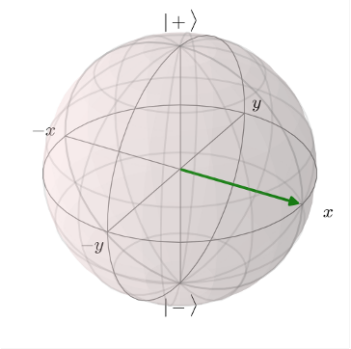

Figure 15: Resultant spin orientation on Bloch Sphere after a 90 degree pulse tip with 0 phase.

Now suppose that we have a first pulse with a relative phase of π. This results in our field being applied along the -y axis, with our spin tipping inverted along the -x axis, shown in Figure 16. Our echo signal is therefore negative. This is true for our second and third sequences.

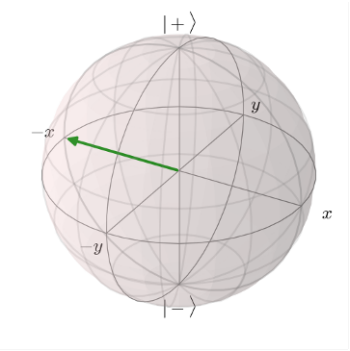

Figure 16: Resultant spin orientation on Bloch Sphere after a 90 degree pulse tip with π relative phase.

It is relatively easy to see that if we are simply concerned with maximizing our echo signal given the phase of our 90 degree pulses, we would need to combine pulse sequence 1 and 4, and then subtract 2 and 3. This assumes we only want echo amplification and does not take into account any reduction in background such as ringdown from our resonators when they interact with a pulse. For our pulse sequences, the last pulse before our echo will always be our 180 degree pulse. To limit noise from ringdown we must consider the relative phase of our 180 degree pulses. In our four scenarios we have either a relative phase of $\frac{\pi}{2}$ or $\frac{3\pi}{2}$. This pulse is responsible for refocusing our spins in the transverse plane, as outlined in 3.8. A phase of $\frac{\pi}{2}$ and $\frac{3\pi}{2}$ changes the direction our spins are rotated around the x-axis - either towards +y or away from it. It does not impact the echo produced in amplitude or sign, it purely refocuses our spins. As a result, we can pick the phase of our 180 degree pulses so that when combined they cancel. The combination that allows this is:

$$(1 + 4) - (2 + 3) \tag{35}$$

Echo signals are amplified, while 180 pulse signal is destroyed. Combining this technique with averaging allows for significant improvement in relative signal strength [23].

5 Methods

5.1 Loop Gap Resonator Design

We use a monomodal LGR for ESR experiments with our high frequency variant, and design a bimodal resonator for heterodimer experiments. The design of the monomodal LGR was principally created using COMSOL Multi-Physics [24] to simulate the LGR inside of a shield with a capacitively coupled antenna. We began by building off of existing designs for Monomodal and Bimodal LGRs. Various parameters, including gap width and loop radius, were changed and simulated. A trial and error process was used to design an LGR with desired Q and resonant frequency. A similar process was followed for both the high frequency monomodal and bimodal LGR. The resonators were machined in the shop from OFHC copper.

5.2 LGR and Sample Probe Tuning

Given the risks of our samples exposure to room temperature and evaporation for extended periods, it is important to have our sample probe and LGR as close to operational as possible before preparing a sample to cool. This process differs for a monomodal and bimodal resonator. The tuning of a monomodal resonator before a sample is introduced is largely the same as the process after the sample is introduced, which is described in section 5.4 in depth. Tuning a bimodal resonator requires additional steps. Given the sensitivity of our bimodal resonator to any changes in positioning in the prongs, it is easy for our two resonance peaks to move as our antenna hits the resonator. Prior to introducing a sample, we insert some sort of dielectric into the main horizontal gap in our resonator. This dielectric serves two main purposes. The first is to pull down our two resonances to our desired range, if necessary. The second is to provide stability to our resonator. Given the proximity of our antenna to the resonator, it is common in making coupling

adjustments to run the antenna into our resonator base. This causes a short, but can also bend the prongs, changing our frequency. A dielectric helps to ensure we limit these changes. A dielectric configuration is tested on bench in an old shield, before being put into our sample probe. Once in the probe, we tune the positioning of our two antennas on the probe to ensure we can see our two resonances again before introducing a sample. This process proved more difficult than expected for the new bimodal resonator design, which will be discussed further in section 7.

5.3 Sample Preparation

As outlined in section 3.4, we can improve coherence times through dilution of our Cr_7Mn in toluene. In this work, we principally work with 10% and 1% concentration samples. The sample preparation process is similar for both. Our high frequency variant of Cr_7Mn has a density of 1.227 g/cc [11]. For a given sample volume, we calculate an appropriate amount of Cr_7Mn volume knowing a desired concentration level. Using our density we can then arrive at an appropriate mass of Cr_7Mn to use. The toluene and Cr_7Mn sample are mixed and allowed to sit. A sample tube made of Suprasil is sealed on one end with a gas-air torch. The diluted sample is placed into the sample tube using a syringe, with wax placed on the top end to seal the sample and limit evaporation effects on dilution.

5.4 Cooling Sample

Outside of the cryostat, a small amount of grease is applied to the inside of our loop in the LGR. The sample tube is then placed into the loop of the LGR, positioned upright and extending out of the loop, as shown in Figure 17. The LGR is screwed into the base of the copper shield. Importantly, the LGR sits on top of two nylon washers at the bottom of the shield to prevent any shorting of the LGR, also shown in Figure 17.

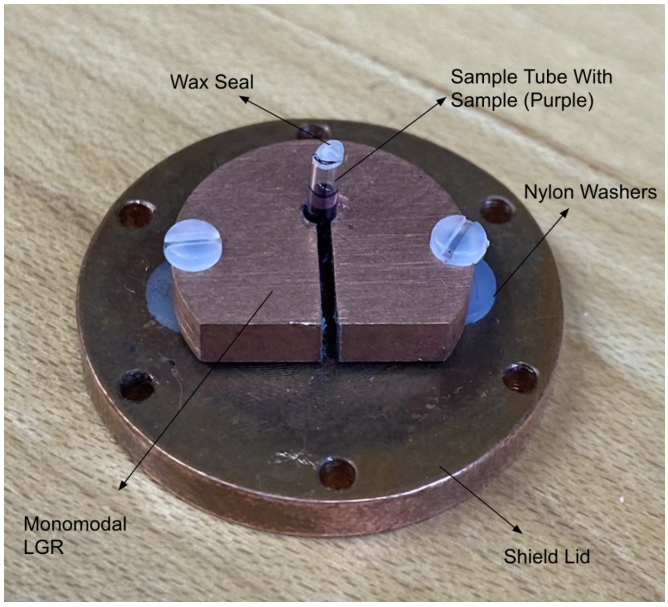

Figure 17: A monomodal LGR with sample. Note that sample tube is sealed with wax and LGR separated from copper base with washers to prevent shorting.

The coax, acting as an antenna, is placed through one of three holes in the top of the shield cap. This positioning depends on the coupling of the antenna to the resonator base. For an inductively coupled configuration, the antenna is bent into a loop and then soldered to the outer portion of copper on the coax. This loop is then dropped directly over the sample tube to inductively couple with the loop of the LGR. The second configuration is a more traditional capacitive coupling. The antenna is bent to a right angle and positioned through the shield to sit over the gap of the LGR. Both configurations were used in our characterization experiments.

The shield cap screws into the shield base, with the antenna positioned as desired. The VNA is used to determine an initial coupling position on bench at room temperature. This is done by reading Smith chart responses on the VNA [25]. The antenna is raised or lowered with respect to the LGR using the micrometers attached to each of the sample probes. For our bimodal

resonator, both antennas are positioned to generate a reasonable coupling. Once reasonably coupled, we prepare our cryostat chamber by pumping and flushing helium. The entire sample probe is lowered into the cryostat chamber while actively flowing helium to limit air from entering the chamber. Air, if allowed in the chamber, will freeze to the sides, acting as an insulator for the sample and limiting cooling power. The cryostat, once sealed with sample and probe inside, begins cooling to 3 K for initial experiments while continuing to pressurize the chamber with helium.

VNA measurements are used to tune the coupling and frequency of the LGR at low temperatures. Relative positioning of the antenna using the micrometer, as well as positioning of the coax connecting the sample probes to the VNA and Spectrometer hardware are the principle variables to change coupling. Initial resonance estimates are seen through dips in the reflected power on the VNA [21]. The goal is to over couple our antenna to the LGR, as measured by the VNA Smith chart [25]. Over coupling will allow us to have a lower Q. We were only able to achieve over coupling on occasion and with less regularity than was initially desired. Reasons for this and potential solutions are discussed at the end of this paper.

5.5 Characterization

To ensure we are still coupled and at an appropriate resonant frequency, a pulsed frequency sweep is conducted once the sample is cold. We send various frequency RF pulses down our antenna and read out the responses of the LGR. The signal is plotted as a function of frequency, which is used to find an appropriate resonance and Q.

A pulse sweep experiment is run to determine an appropriate pulse length to ensure we are tipping our spins roughly 90 degrees. Once an initial guess at a 90 degree pulse is found, a rabi sweep is run to determine an adequate nutation pulse length. With an appropriate nutation pulse to invert our spins, an inversion sweep allows for us to measure a T_1 for the system. A

Hahn echo sweep is run to measure T_2.

We need to understand how our signal behaves at various field strengths to confirm that we are operating at a clock transition. A field sweep experiment is run to test this. We apply a longitudinal field B_0 of various strengths and readout the signal from our pulse sequence. In theory, we expect that if we are on a clock transition, this signal should be strongest at 0 field, before falling off rapidly at higher fields.

A frequency sweep is run as a final experiment. This sweep sends down our pulse sequence at varying frequencies. We would expect to see a response centered around our resonators resonance. As our frequency moves past this resonance our pulse widths and delays will no longer be appropriate to generate an echo signal. If we have a sample transition frequency which has a narrow response and is off frequency from our resonator resonance, we might expect a separate signal away from our resonator's resonance.

6 Results

6.1 Loop Gap Resonators

We successfully designed two different loop gap resonators. Our monomodal LGR, shown on the right in Figure 18, is operational at room temperature with no sample at 5.545 GHz based on VNA testing. This LGR was designed based on existing models with the front portion of the outer radius cut off, as shown in Figure 18.

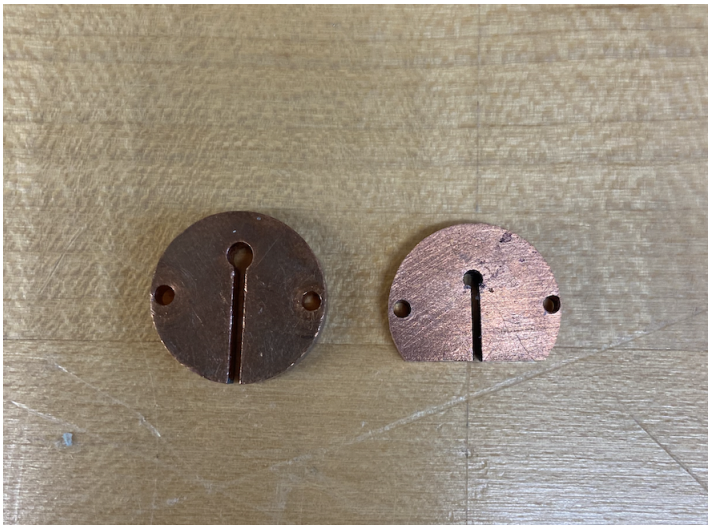

Figure 18: New high frequency monomodal LGR (Right) compared to existing low frequency monomodal LGR (Left). Main design difference allowing for higher frequency is cut-off creating shorter gap and resonator body.

A second LGR was designed to operate at two distinct frequencies. Our design has a unique characteristic of having different lengths on each of the four prongs which form the two perpendicular gaps. This design is shown in Figure 19. It is simulated to operate at approximately 4.93 and 6.26 GHz.

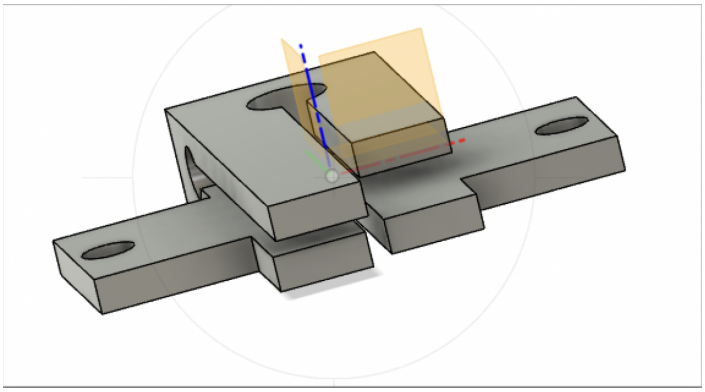

Figure 19: Design schematic of Bimodal LGR. Note varying lengths of four "prongs". Simulated to operate at approximately 4.93 and 6.26 GHz. Full drawing in Appendix A.

The bimodal LGR, once machined, was operational at $\sim$ 4 and $\sim$ 5.3 GHz. The resonant frequencies are more variable given the fragile nature of the four prongs shown in Figure 20.

Figure 20: New bimodal resonator shown on copper shield cap. Resonant Frequencies are variable with bending of prongs. Generally around 4 and 5.3 GHz.

6.2 10 Percent Concentration High Frequency Variant at 3 K

Our monomodal LGR was used to characterize our high frequency variant energy transitions for our monomer. At 3 K, a pulsed frequency sweep finds that our resonator is operating at 5.21 GHz. This sweep is shown in Figure 21.

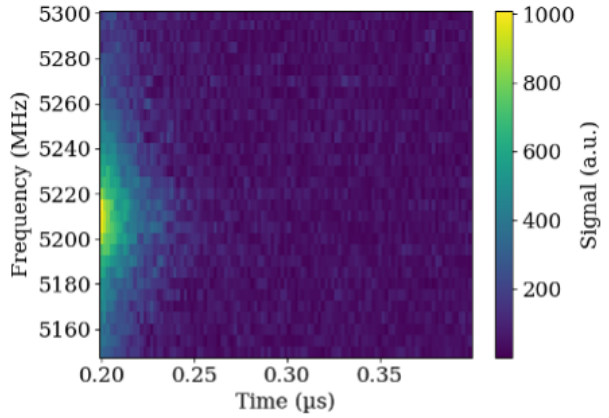

Figure 21: High frequency monomer variant pulsed frequency sweep with high frequency monomodal resonator at 3 K. 50 ns pulse width and 100 μs rep. time. Strong response shown with center at 5210 MHz.

A pulse sweep showed weak signal around 100 ns. This is applied as our main 90 degree pulse width for future experiments. With a 100 ns pulse width, a rabi sweep is run with results shown in Figure 22.

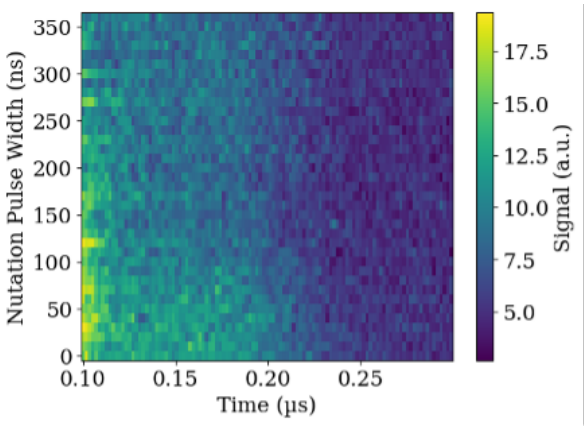

Figure 22: High frequency variant monomer rabi sweep at 3 K and 5210 MHz, using high frequency monomodal LGR. 100 ns pulse width, 500 μs echo delay, 5 μs nutation delay, 500 μs rep. time. Shows some weak oscillations with an appropriate nutation pulse width found at 200 ns.

Figure 22 shows weak rabi oscillations with a potentially low signal around 200 ns. This pulse width is applied as a nutation pulse for our inversion sweep.

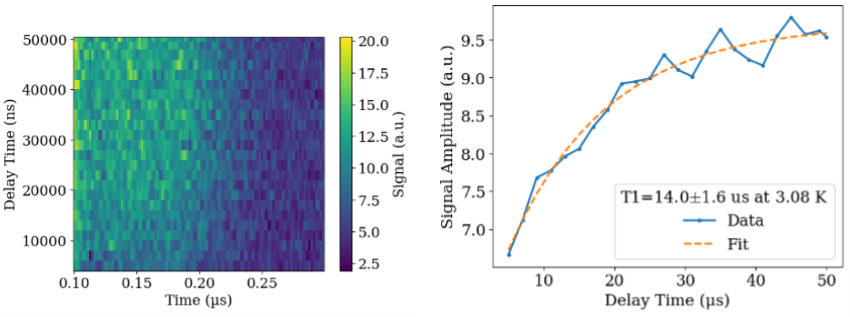

(a) (b)

Figure 23: High frequency monomer inversion sweep (a) and corresponding T_1 exponential fit with T_1 constant (b). Used high frequency monomodal LGR. Run at 3 K, 5210 MHz with 100 μs rep. time, 200 ns nutation pulse, 250 ns delay and 100 ns pulse width.

An inversion sweep is shown in Figure 23, along with the corresponding fit for our T_1. We measure a T_1 of 14.0 ± 1.6 μs. Using a Hahn echo sweep

we measure a T_2 of 203 ± 16 ns, as shown in Figure 24.

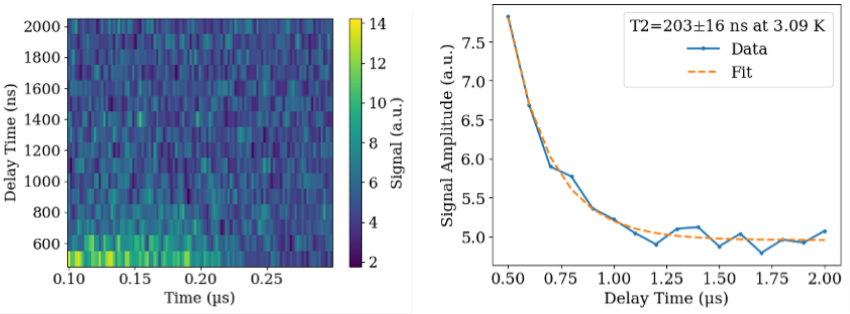

(a) (b)

Figure 24: High frequency variant monomer Hahn echo sweep (a) and corresponding T_2 decay fit with T_2 constant. Used high frequency monomodal LGR. Run at 3 K, 5210 MHz with 100 μs rep. time, and 100 ns pulse width.

Field and frequency sweeps are shown in Figure 25. Our field sweep does not show significant dependence on field nor a strong signal at 0 field falling off. Our frequency response shows a strong signal centered on our resonant frequency.

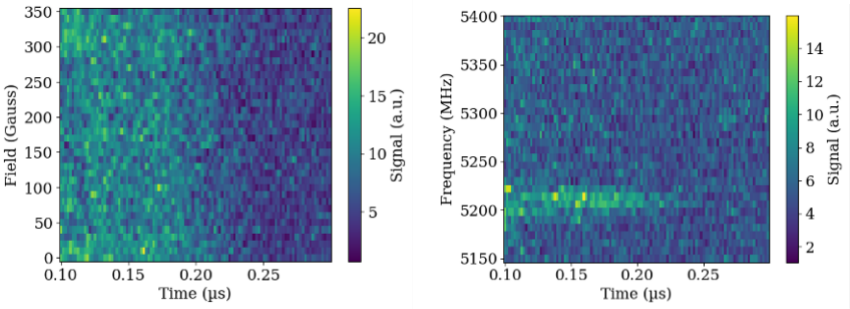

(a) (b)

Figure 25: High frequency variant monomer field sweep (a) and frequency sweep (b) results. Run with same parameters as prior 3 K tests. Used high frequency monomodal LGR. Field sweep shows fairly constant signal rather than signal concentrated at 0 field as was expected.

6.3 10 Percent Concentration High Frequency Variant at 1.5 K

A pulsed frequency sweep at 1.3 K gives a strong response from the resonator at 5220 MHz, shown in Figure 26.

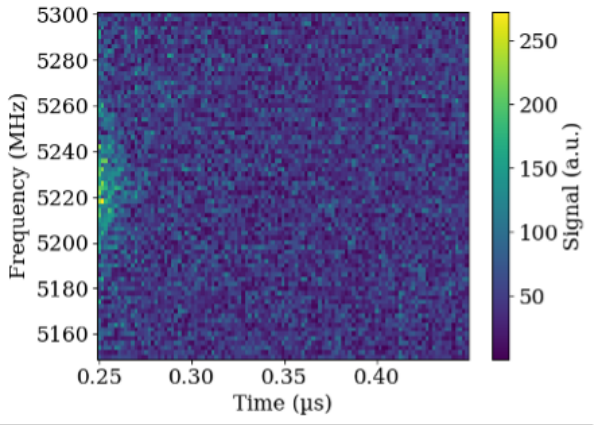

Figure 26: High frequency variant monomer pulsed frequency sweep with high frequency monomodal resonator showing response centered at 5220 MHz. 1.5 K with 50 ns pulse, 100 ns rep time. Weaker signal and broader bandwidth demonstrates a lower Q.

A pulse sweep found a similar weak signal at 120 ns as with the higher temperature experiments. A rabi sweep ran with this pulse width gave strong evidence of Rabi oscillations, shown in Figure 27.

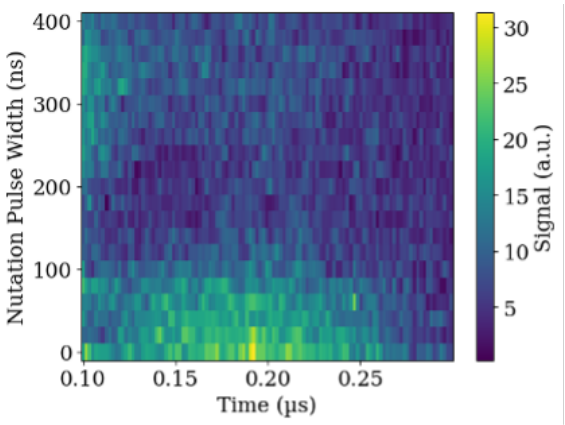

Figure 27: High frequency variant monomer rabi sweep run at 1.5 K and 5220 MHz. 120 ns pulse width, 800 ns nutation delay, 300 ns delay, 200 μs rep. time. Used high frequency monomodal LGR. Shows distinctly low signal at 200 ns indicating an appropriate nutation pulse width.

An inversion sweep with a nutation pulse width of 200 ns gave a T_1 of $11.8 \pm 1.5 \mu s$, shown in Figure 28.

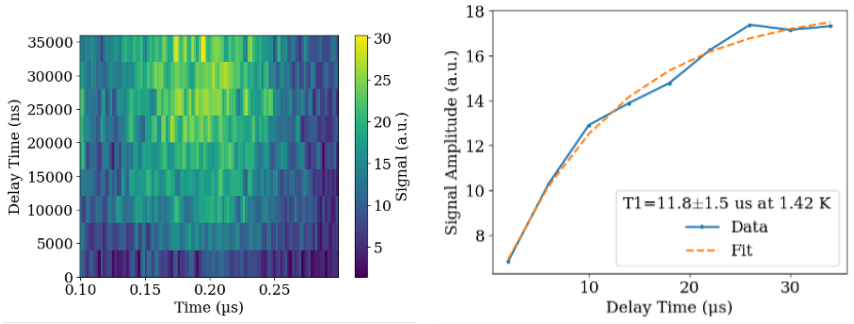

(a) (b)

Figure 28: High frequency monomer inversion sweep (a) and corresponding T_1 exponential fit with T_1 constant (b). Used high frequency monomodal LGR. Run at 1.5 K and 5220 Mhz with 120 ns pulse, 300 ns delay, 200 ns nutation pulse and 200 μs rep time.

Our T_2 from a Hahn echo sweep was measured to be 305 ± 28 ns, shown in Figure 29.

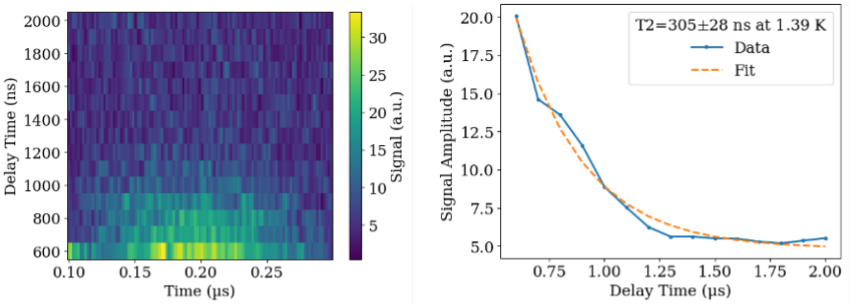

(a) (b)

Figure 29: High frequency variant monomer Hahn echo sweep (a) and corresponding T_2 decay fit with T_2 constant. Used high frequency monomodal LGR. Run at 1.5 K and 5220 MHz with 120 ns pulse and 200 ns rep time.

Field dependence is as expected, with strong signal near zero field and falling off at higher field, shown in Figure 30. We again see frequency sweep responses centered on our resonant frequency, as expected, also shown in Figure 30.

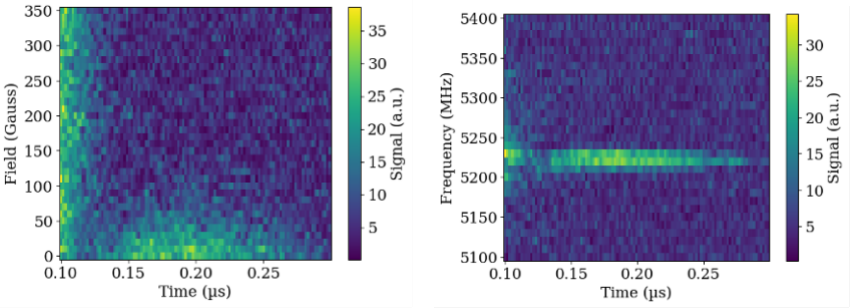

(a) (b)

Figure 30: High frequency variant monomer field sweep (a) and frequency sweep (b) results. Used high frequency monomodal LGR. Run with same parameters as prior 1.5 K tests. Field sweep is as expected with signal concentrated at 0 field.

6.4 1 Percent Low Frequency Variant at 3 K

Before beginning characterization of our Dimer sample, we revisited our lower frequency monomer to verify results found in prior research. We looked exclusively at a 1% concentration of this variant. An initial pulsed frequency sweep using our low frequency monomodal LGR showed a resonator response around 4087 MHz, as shown in Figure 31.

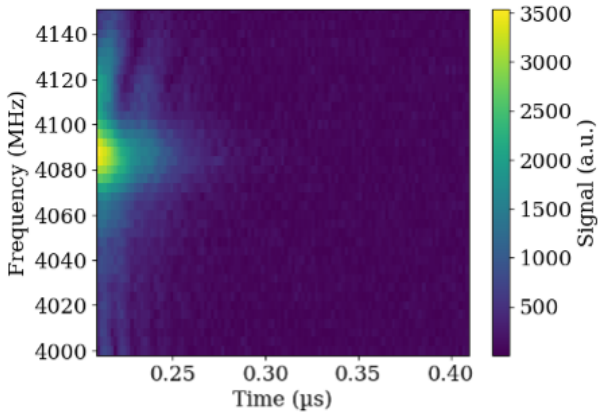

Figure 31: Low frequency variant monomer pulsed frequency sweep with low frequency monomodal resonator showing response centered at 4087 MHz. Sweep taken at 3 K with 50 ns pulse and 100 μs rep. time.

At this frequency, our pulse sweeps showed signal response at 70 ns. We used this pulse width to run a rabi sweep, with rabi oscillations observed and shown in Figure 32.

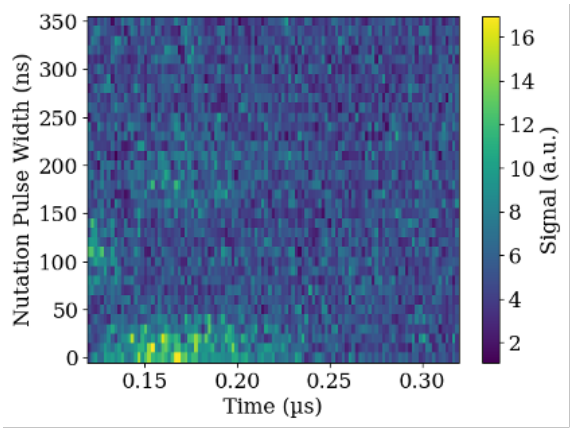

Figure 32: Low frequency variant monomer rabi sweep taken at 3 K and 4087 MHz. Used low frequency monomodal LGR. 70 ns pulse width, 800 ns nutation delay, 300 ns delay, 200 μs rep. time. Indicates nutation pulse width of 100 ns.

The rabi sweep also suggests an appropriate nutation pulse width of 100 ns. Using this, we ran an inversion sweep to measure a T_1 time constant. This is shown in Figure 33. Note that here we are plotting the quadrature of our signal, rather than the amplitude, due to poor signal to noise quality on our amplitude channel. This leads to the inverted signal in (a) and the inverted fit in (b). We measure a T_1 of 36 ± 3 μs. This is roughly in line with prior work done by [3] measuring a value of 28μs at 10% dilution.

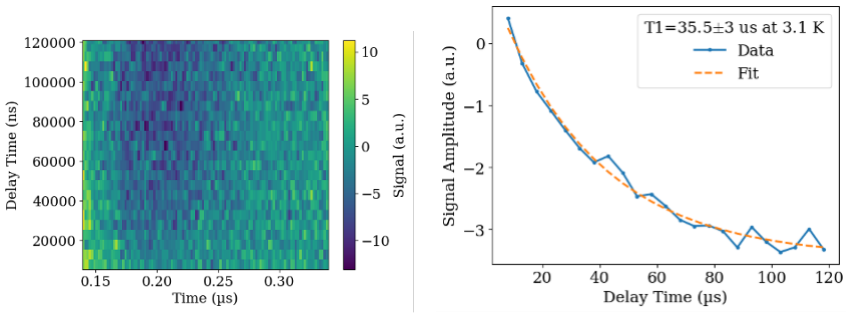

(a) (b)

Figure 33: Low frequency variant monomer inversion sweep (a) and T_1 fit (b). Used low frequency monomodal LGR. Run at 3 K and 4087 MHz with 70 ns pulse, 100 ns nutation pulse, 300 ns delay and 200 μs rep. time.

A Hahn echo sweep shown in Figure 34 and corresponding fit measured a T_2 time constant of 243 ± 25 ns, below a previously measured 390 ns [3].

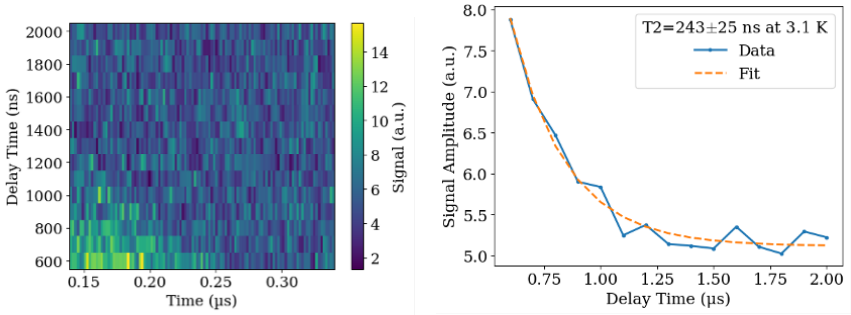

(a) (b)

Figure 34: Low frequency variant monomer Hahn echo sweep (a) and T_2 fit with T_2 time constant (b). Used low frequency monomodal LGR. Run at 3 K and 4087 MHz with 70 ns pulse, 300 ns delay and 200 μs rep. time.

Field dependence is as expected, with all signal concentrated at zero field before falling off at higher fields. Signal response is concentrated around the resonant frequency, as expected. Both results are in line with previous characterization and are shown in Figure 35.

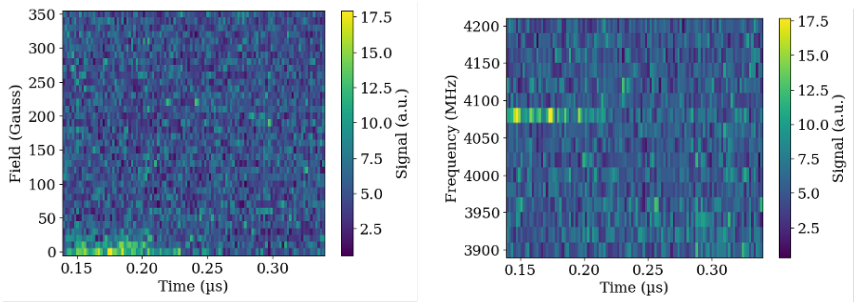

(a) (b)

Figure 35: Low frequency variant monomer field sweep (a) and frequency sweep (b). Used low frequency monomodal LGR. Same parameters as prior sweeps with signal response as expected.

6.5 1 Percent Low Frequency Variant at 1.5 K

We also verified a prior characterization of our low-frequency variant at 1.5 K. A pulsed frequency sweep using the same LGR showed a response at 4080 MHz, shown in Figure 36.

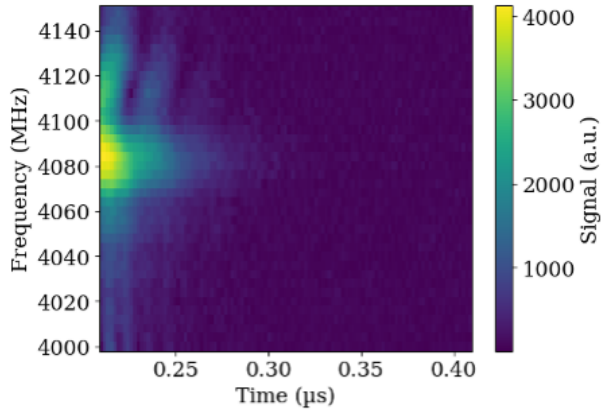

Figure 36: Low frequency variant monomer pulsed frequency sweep with low frequency monomodal showed response at 4080 MHz. Sweep at 1.5 K with 50 ns pulse and 100 μs rep. time.

A pulse sweep showed signal around 80 ns in pulse width. This pulse was

applied in a rabi sweep, where we observed rabi oscillations and a nutation pulse width of 100 ns, shown in Figure 37.

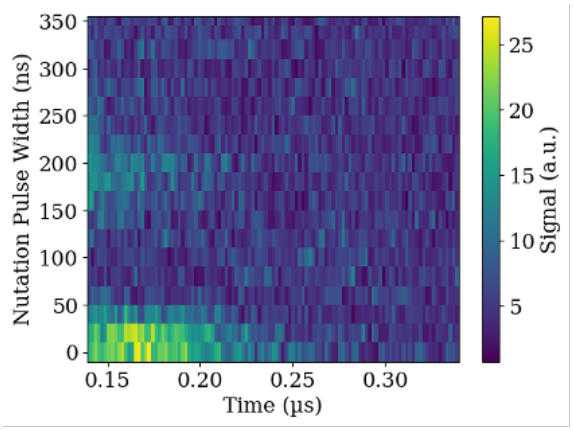

Figure 37: Low frequency variant monomer rabi sweep at 1.5 K and 4080 MHz. 80 ns pulse width, 800 ns nutation delay, 300 ns delay and 200 μs rep. time. Shows nutation pulse width of 100 ns.

In this characterization, we were unable to measure a T_1 accurately through an inversion sweep. It is unknown why this was the case, but likely the result of some apparatus error. We do not believe this was the result of any larger changes in our sample given the consistent behavior through other tests and at other temperatures.

We measure a T_2 of 283 ± 28 ns from a Hahn echo sweep, as shown in Figure 38. This is below previously measured values at 0.5% concentration of 390 ns [1].

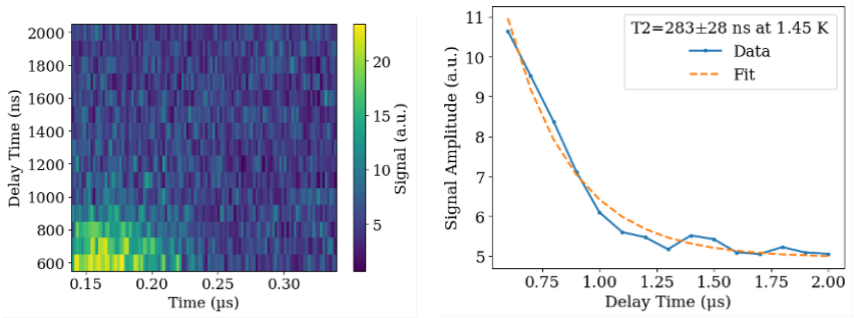

(a) (b)

Figure 38: Low frequency variant monomer Hahn echo (a) and corresponding T_2 fit (b). Used low frequency monomodal LGR. Sweep taken at 1.5 K and 4080 MHz. 80 ns pulse width, 300 ns delay and 200 μs rep. time.

Field dependence and frequency response both remained consistent at 1.5 K, again in line with prior experiments, shown in Figure 39.

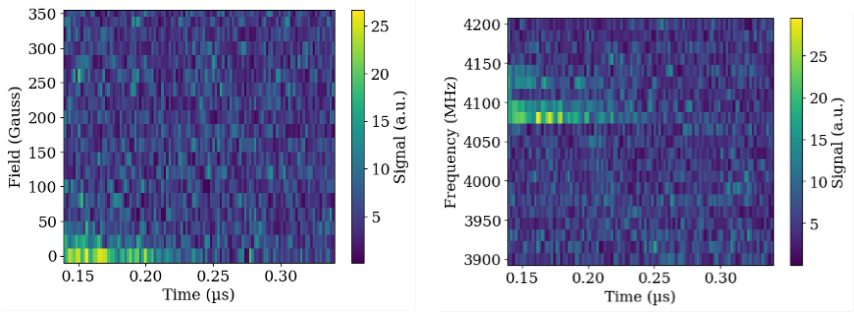

(a) (b)

Figure 39: Low frequency variant monomer field sweep (a) and frequency sweep (b). Used low frequency monomodal LGR. Both taken with same parameters as prior sweeps with results as expected.

6.6 Low Frequency in Dimer at 3 K

The second half of our research explored the behavior of our heterodimer sample. Characterization began with understanding the behavior of each of our individual spin systems within our dimer. We used two monomodal

resonators during separate cool downs for this characterization, starting with our lower frequency monomodal LGR to understand the behavior of our low frequency spin system in our dimer.

A pulsed frequency sweep showed a response at 4000 MHz, shown in Figure 40.

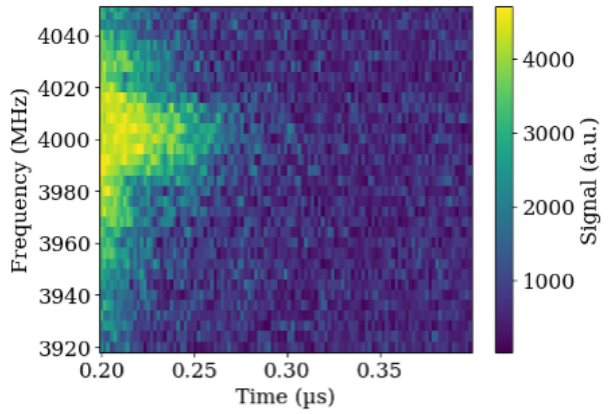

Figure 40: Low frequency variant in dimer pulsed frequency sweep using low frequency monomodal LGR showing response centered at 4000 MHz. Sweep run at 3 K with 50 ns pulse and 100 μs rep. time.

A pulse sweep showed strong signal at a 60 ns pulse width, which was used to run a rabi sweep, which demonstrated rabi oscillations - shown in Figure 41. This behavior is consistent with our low frequency monomer behavior.

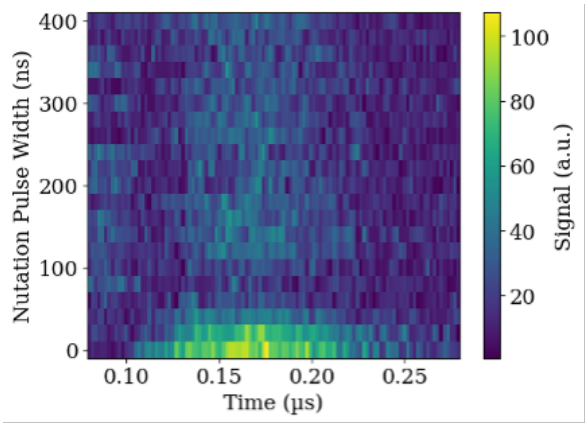

Figure 41: Low frequency variant in dimer rabi sweep at 3 K and 4000 MHz. Used low frequency monomodal LGR. 60 ns pulse width, 800 ns nutation delay, 200 ns delay and 60 μs rep. time. Shows nutation pulse width of 90 ns.

Using an appropriate nutation pulse width of 90 ns, an inversion sweep and corresponding T_1 fit, we measured a T_1 of 9.7 ± 2 μs, shown in Figure 42. This is significantly below our 1% concentration value of 36 ± 3 μs. We are not sure why this might be happening and need more tests to confirm a discrepancy.

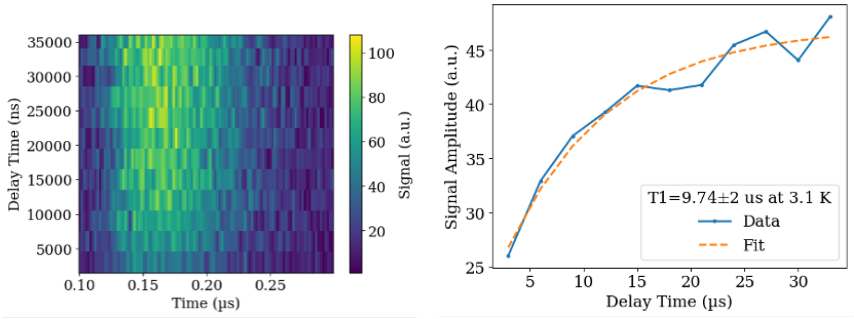

(a) (b)

Figure 42: Low frequency variant in dimer inversion sweep (a) and corresponding T_1 fit (b). Used low frequency monomodal LGR. Taken at 3 K and 4000 MHz. 60 ns pulse, 90 ns nutation pulse, 200 ns delay, 60 μs rep. time.

A Hahn echo sweep and T_2 fit measured a T_2 of 242 ± 20 ns, shown in Figure 43. This is in line with 1% low frequency variant monomer values of 243 ± 25 ns found in section 6.4. We would expect that the higher dilution level increase coherence times, even in a dimer. This is discussed further in section 7.

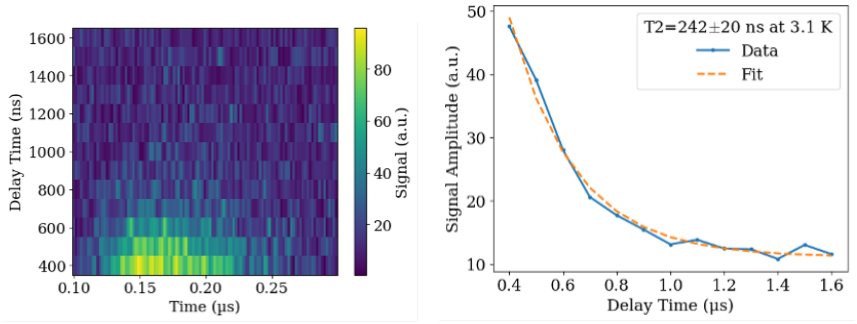

(a) (b)

Figure 43: Low frequency variant in dimer Hahn echo sweep and corresponding T_2 fit. Used low frequency monomodal LGR. Taken at 3 K and 4000 MHz. 60 ns pulse, 200 ns delay, 60 μs rep. time.

We found field dependence and signal frequency response as expected, shown in Figure 44.

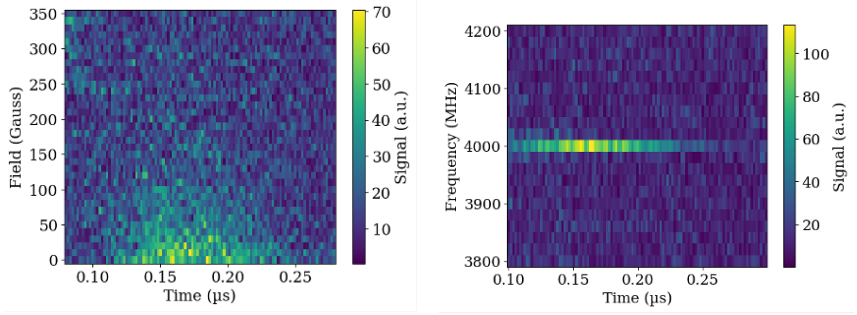

(a) (b)

Figure 44: Low frequency variant in dimer field sweep (a) and frequency sweep (b). Used low frequency monomodal LGR. Taken with same parameters as prior sweeps showing expected behavior.

6.7 Low Frequency in Dimer at 1.5 K

At 1.5 K, we observe a strong response from our low frequency monomodal LGR centered at 3968 MHz for a pulsed frequency sweep, shown in Figure 45.

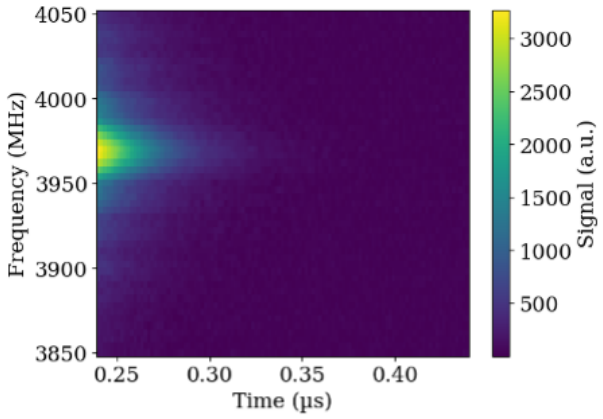

Figure 45: Low frequency variant in dimer pulsed frequency sweep with low frequency monomodal LGR showing response at 3968 MHz. 50 ns pulse width and 100 μs rep. time.

A pulse sweep finds a 55 ns pulse width, which is used to demonstrate rabi oscillations, shown in Figure 46. This is similar to rabi oscillations seen in our low frequency monomer experiments.

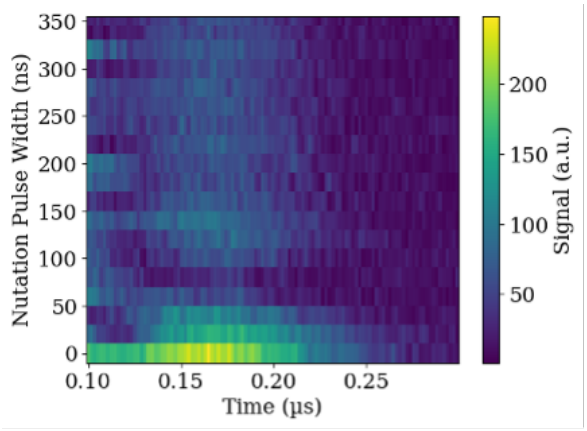

Figure 46: Low frequency variant in dimer rabi sweep at 1.5 K and 3968 MHz. Used low frequency monomodal LGR. 55 ns pulse width, 800 ns nutation delay, 200 ns delay and 100 μs rep. time. Shows nutation pulse width of 90 ns.

Applying a nutation pulse of 90 ns, an inversion sweep is run to measure a T_1 constant of 12.8 ± 4 μs, shown in Figure 47.

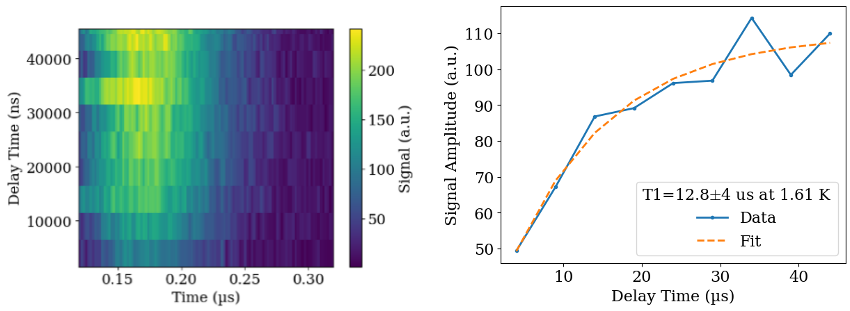

(a) (b)

Figure 47: Low frequency variant in dimer inversion sweep (a) and corresponding T_1 fit (b). Used low frequency monomodal LGR. Taken at 1.5 K and 3968 MHz. 55 ns pulse, 90 ns nutation pulse, 200 ns delay, 100 μs rep. time.

A Hahn echo sweep and corresponding fit measured a T_2 of 286 ± 9.8 ns, shown in Figure 48. This is below values of 390 ns in the low frequency

monomer found by [1]. It is in line with the measured value in the 1% low frequency monomer of 283 ± 28 ns in section 6.5.

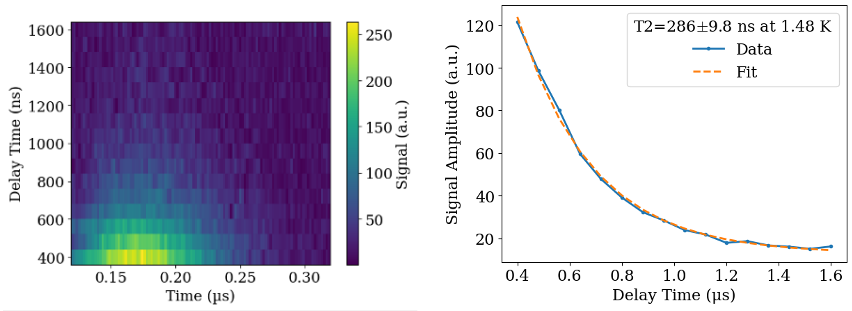

(a) (b)

Figure 48: Low frequency variant in dimer Hahn echo sweep and corresponding T_2 fit. Used low frequency monomodal LGR. Taken at 1.5 K and 3968 MHz. 55 ns pulse, 200 ns delay, 100 μs rep. time

Field behavior was as expected. Note that in Figure 49, we have a more narrow sweep range than in previous frequency sweeps. Both of these tests are in line with behavior we observed in our monomer for this variant.

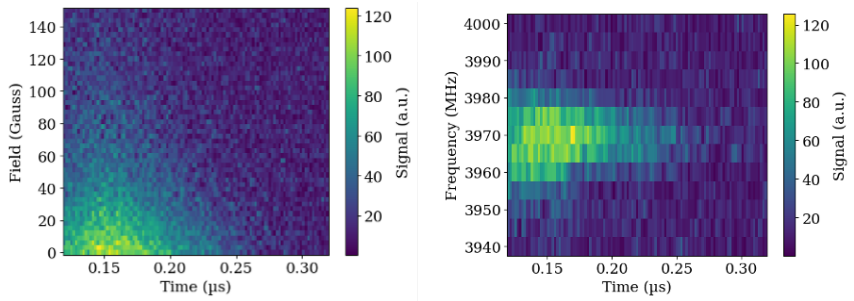

(a) (b)

Figure 49: Low frequency variant in dimer field sweep (a) and frequency sweep (b). Used low frequency monomodal LGR. Taken with same parameters as prior sweeps showing expected behavior.

6.8 High Frequency in Dimer at 3 K

Using our higher frequency monomodal LGR we looked at the higher frequency variant within our dimer at both temperatures. A pulsed frequency sweep shows a response centered at 5275 MHz in Figure 50.

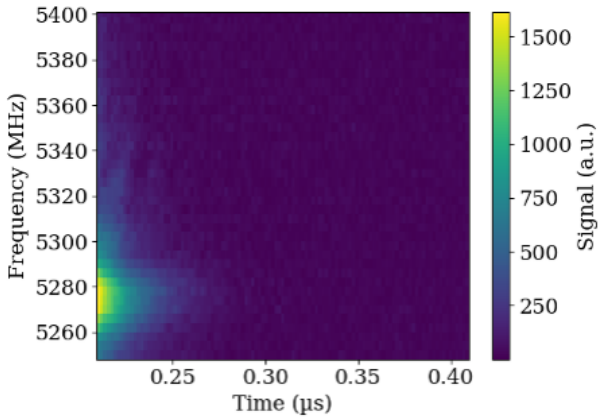

Figure 50: High frequency variant in dimer pulsed frequency sweep with high frequency monomodal LGR taken at 3 K showing response at 5275 MHz. 50 ns pulse width and 100 μs rep. time.

A 120 ns pulse width is found from a pulse sweep and used in a rabi sweep shown in Figure 51 demonstrating rabi oscillations, similar to what we saw in our monomer sample.

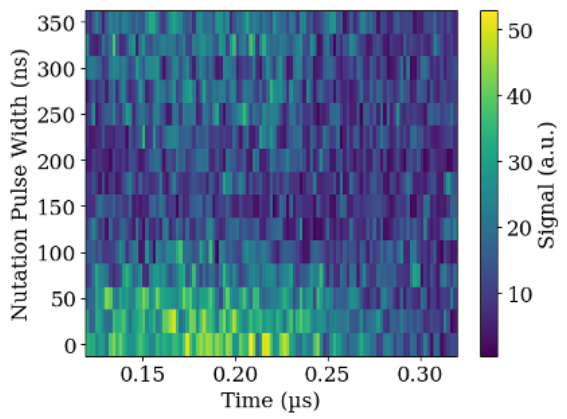

Figure 51: High frequency variant in dimer rabi sweep at 3 K and 5275 MHz. Used high frequency monomodal LGR. 120 ns pulse width, 800 ns nutation delay, 300 ns delay and 200 μs rep. time. Shows appropriate nutation pulse width of 150 ns.

An inversion sweep and corresponding fit gives a T_1 measurement of 5.9 ± 0.6 μs, shown in Figure 52. This value is significantly below our 10% high frequency monomer value of 14.0 ± 1.6 μs.

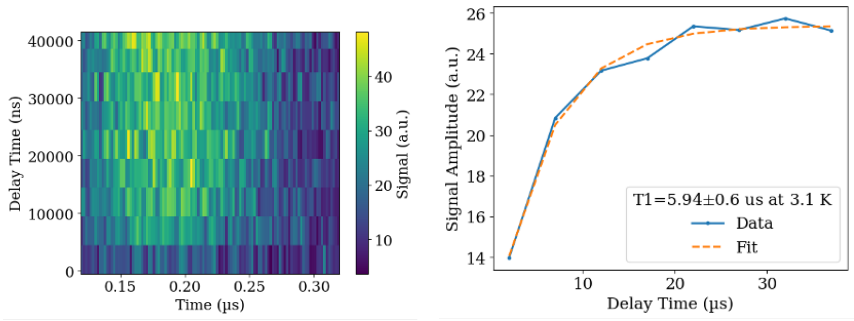

(a) (b)

Figure 52: High frequency variant in dimer inversion sweep (a) and T_1 fit (b) taken at 3 K and 5275 MHz. Used high frequency monomodal LGR. 120 ns pulse, 150 ns nutation pulse, 300 ns delay and 200 μs rep. time.

From the Hahn echo sweep and fit shown in Figure 53, we measure a T_2 of 173 ± 10 ns, below our monomer value of 203 ± 16 ns.

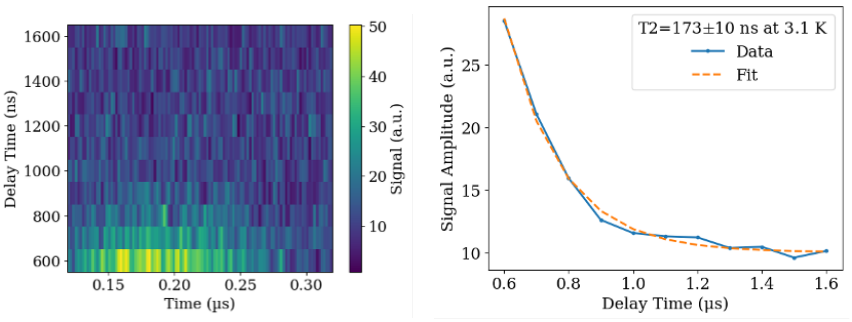

(a) (b)

Figure 53: High frequency variant in dimer Hahn echo sweep (a) and corresponding T_2 fit (b) taken at 3 K and 5275 MHz. Used high frequency monomodal LGR. 120 ns pulse, 300 ns delay and 200 μs rep. time.

Once again, field and frequency signals shown in Figure 54 are as expected. We did not find field behavior as expected in section 6.2, though we expect that we are retaining clock transitions in both the monomer and the dimer.

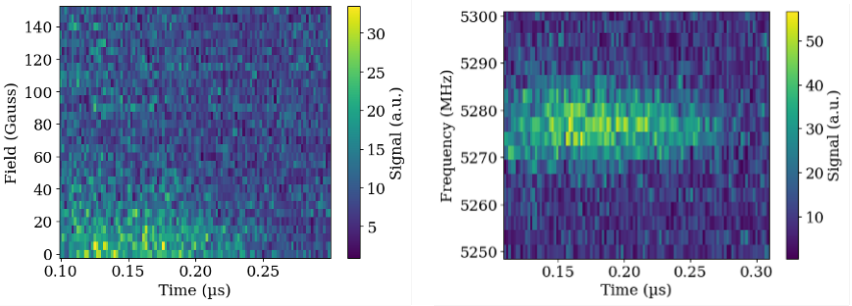

(a) (b)

Figure 54: High frequency variant in dimer field sweep (a) and frequency sweep (b). Used high frequency monomodal LGR. Frequency sweep taken at 5275 MHz with field sweep taken at 5228 MHz - other parameters remained the same. Both responses are as expected.

6.9 High Frequency in Dimer at 1.5 K

At 1.5 K, a pulsed frequency sweep showed a response centered at 5223 MHz, shown in Figure 55.

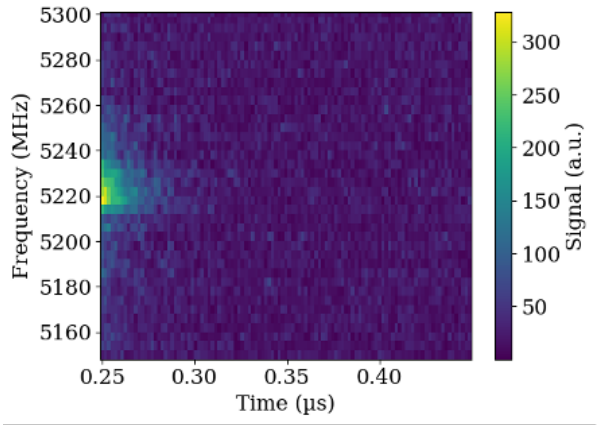

Figure 55: High frequency variant in dimer pulsed frequency sweep at 1.5 K showing response at 5223 MHz. Used high frequency monomodal LGR. 50 ns pulse width and 100 μs rep. time.

At this frequency, a pulse sweep measured a pulse width of 130 ns, which was used in the rabi sweep shown in Figure 56, again showing rabi oscillations similar to our monomer measurements.

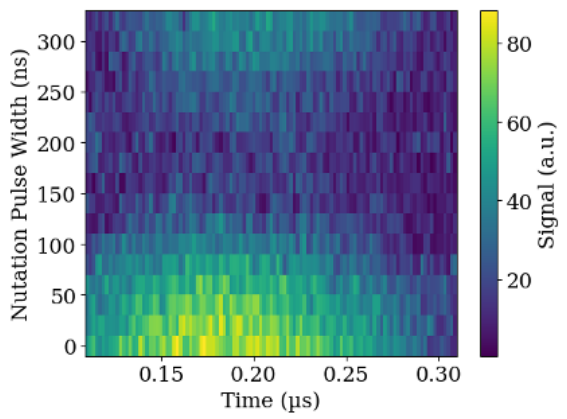

Figure 56: High frequency variant in dimer rabi sweep taken at 1.5 K and 5223 MHz. Used high frequency monomodal LGR. 130 ns pulse width, 800 ns nutation delay, 300 ns delay and 200 μs rep. time. Shows appropriate nutation pulse width of 175 ns.

Using a nutation pulse width of 175 ns and the inversion sweep shown in Figure 57, we measure a T_1 of 19 ± 4 μs, which is slightly above our monomer value at 1.5 K of 11.8 ± 1.5 μs, though closer than our 3 K values.

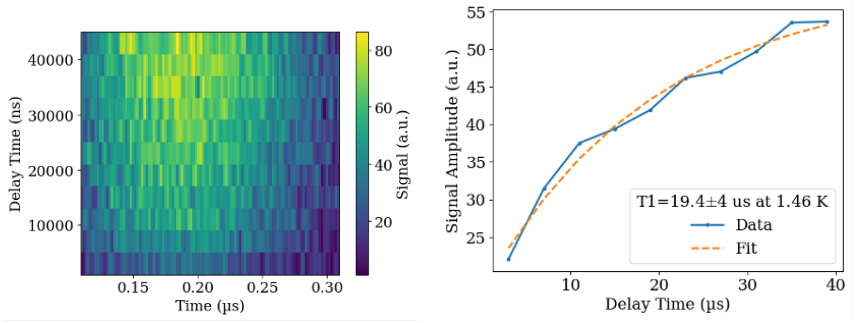

(a) (b)

Figure 57: High frequency variant in dimer inversion sweep (a) and T_1 fit (b) taken at 1.5 K and 5223 MHz. Used high frequency monomodal LGR. 130 ns pulse, 175 ns nutation pulse, 300 ns delay and 200 μs rep. time.

A Hahn echo sweep and fit finds a T_2 of 253 ± 7 ns as shown in Figure 58, again below our monomer value of 305 ± 28 ns.

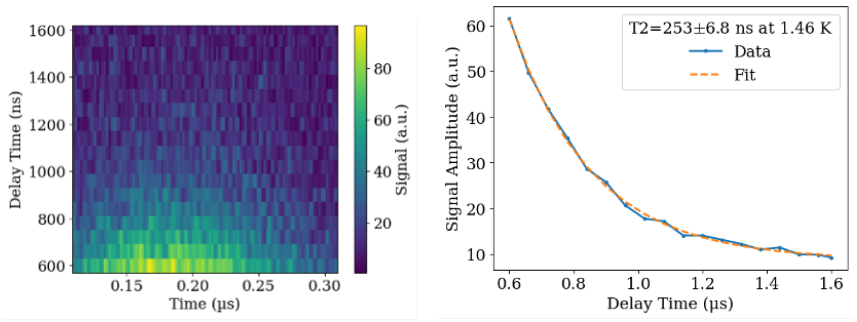

(a) (b)

Figure 58: High frequency variant in dimer Hahn echo sweep (a) and T_2 fit (b) at 1.5 K and 5223 MHz. Used high frequency monomodal LGR. 130 ns pulse, 300 ns delay and 200 μs rep. time.

Field and frequency signal responses are as expected, shown in Figure 59, and both behaved similarly to our monomer measurements.

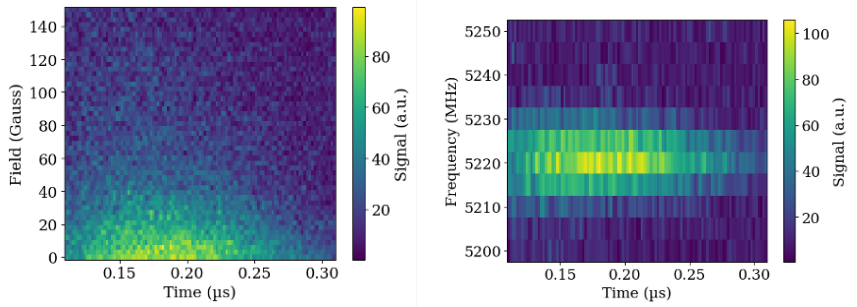

(a) (b)

Figure 59: High frequency variant in dimer field sweep (a) and frequency sweep (b) taken with same parameters as above at 1.5 K. Used high frequency monomodal LGR. Both show expected results.

6.10 Initial Results for 10% Dimer at 3 K Using Bimodal LGR

We began the process of implementing our newly built bimodal LGR to drive transitions at both frequencies in the same experiment. At 3 K we saw

the frequency response shown in Figure 60, with our resonance centered at 5150 MHz. This plot is focused on our high frequency response with one antenna. A separate response from our second probe is found around 3700 MHz, not shown given its inconsistent behavior, as described below.

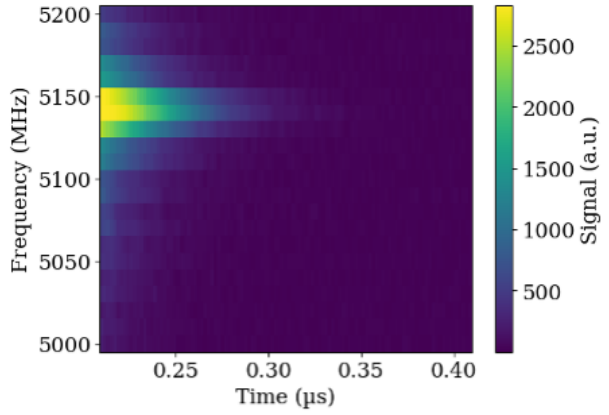

Figure 60: Dimer pulsed frequency sweep using bimodal resonator at 3 K showing response at 5150 MHz 50 ns pulse width and 100 μs rep. time.

We ran a pulse sweep at this frequency to verify that we had signal from our high frequency variant. Figure 61 shows signal, confirming that we are able to drive our high frequency transition.

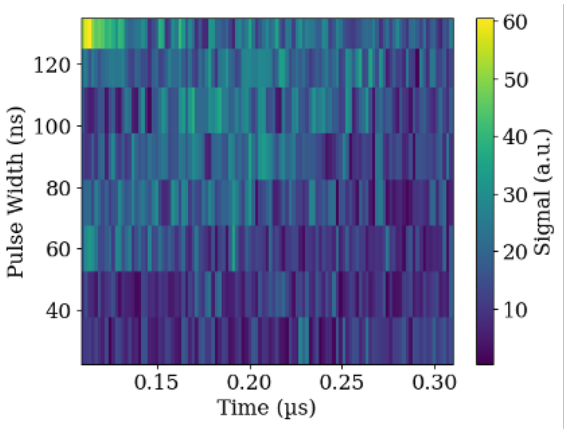

Figure 61: Dimer pulse sweep at 3 K and 5150 MHz. 300 ns delay, 200 μs rep. time. Used bimodal resonator. Shows signal concentrated at 100 ns pulse width and 0.20 μs. Strong signal shown in top left is ringdown noise from long pulse lengths.

During this cool down we were unable to detect signal at our lower frequency transition, largely due to our resonant frequency for our lower mode changing during the experiments - which we discuss further in section 7.

In a separate cool down we were able to see more stable frequency responses at 5300 and 3940 MHz, shown in Figure 62. While these frequencies are centered where we expect to manipulate our spin system, we were unable to see signal at either frequency. We are not sure why this may have been the case at this point.

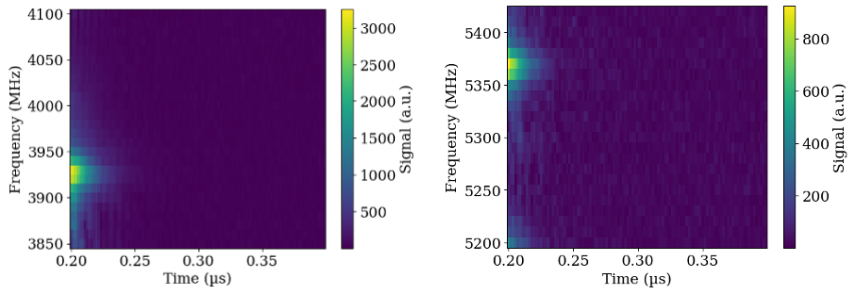

(a) (b)

Figure 62: Dimer pulsed Frequency responses using bimodal resonator showing responses at 3930 MHz (a) and 5375 MHz (b). Both at 3 K with 50 ns pulse width and 100 μs rep. time. Associated Q of 300 and 250.

7 Discussion and Conclusion

Our results confirm that it is possible to manipulate a heterodimer of Cr_7Mn. By designing an operational high frequency monomodal LGR we are able to detect signal for the high frequency monomer as well as both variants in the dimer using ESR. A new bimodal LGR allows for resonance at 5300 and 3950 MHz simultaneously.

Our 10% high frequency sample showed mixed results. We successfully measure initial estimates for both T_1 and T_2. At 3 K we measure a T_1 of 14.0 ± 1.6 μs, and at 1.5 K we measure a T_1 of 11.8 ± 1.5 μs. Our T_2 at 3 K is 203 ± 16 ns and at 1.5 K is 305 ± 28 ns. Our T_2 values at 1.5 K are slightly shorter than previously found T_2 for the low frequency variant of 380 ns [1]. Our T_1 was similar to previously measured low frequency values [1]. Our signal at 3 K was relatively weak, with indistinct rabi oscillations. This is likely due to our short T_2 and high Q. Furthermore, we find that our sample does not respond to variations in longitudinal field strength as expected. We find some signal response at high field. Operating at a clock transition means that signal response should be strongest at 0 field and fall off rapidly at higher fields. A potential cause for these issues could have been with our antenna-

resonator set up. Our antenna was inductively coupled with our LGR but overcoupling was inconsistent. We believe our antenna at was hitting our resonator itself during in-situ adjustments, causing soldering joints to break and leading to a noisy signal near the end of 10% characterization at high temperatures. We resolved this issue by adding a hole in the bottom of our shield, allowing our sample tube to sit lower and flush with the top of the resonator in later experiments.

Characterization of our 10% high frequency sample at low temperature was more conclusive. We find a longer T_2 time, consistent with increased coherence at lower temperatures. In addition, we observed more distinct rabi oscillations and a significantly improved field signal, strong indications that we are indeed operating on a clock transition.

Our characterization for our low frequency variant at 1% found mixed results compared to prior work by [1] performed at 10% and 0.5% concentrations. We were able to experimentally verify that we are operating on a clock transition given field dependence. However, we found T_2 measurements below prior measurements (283 vs. 390 ns. This variation could be due to differences in dilution or other sample preparation procedures.

We also began characterization of our dimer sample at 10 % concentration. Using monomodal resonators we explored both the high and low frequency variants within our dimer independently of each other. In our low frequency variant we experimentally verified that we are able to maintain a clock transition within our dimer system. We also show that our coherence time continues to increase at lower temperature within our dimer (242 ns vs. 286 ns). Coherence times for this variant in our dimer were largely in line with our coherence times for our 1% samples in the monomer. All else equal, we would expect for coherence times to be lower at higher concentrations, though it is unclear how the dimer could impact this. As above, our coherence times were on the whole slightly lower than in [1]. We clearly demonstrated the presence of rabi oscillations for our low frequency spin system.

For our high frequency system in the dimer we also show the presence of a clock transition given our field dependence. Coherence times increased at lower temperatures, though at both 1.5 and 3 K our coherence times in the dimer were slightly lower than our measured times in the monomer. At this point, further tests are needed to verify whether this is a physical difference or simply an anomaly perhaps due to fit irregularities. This difference is also likely in part caused by dilution differences. Current estimates for density of our dimer sample are imprecise, leading to the process outlined in section 5.3 being imprecise. Theoretically, we do not expect for there to be a significant falloff in coherence times from a monomer to a dimer, especially given that we still operate on a clock transition.

We were also able to demonstrate that our bimodal resonator is operational around 5.3 and 4 GHz, frequencies which should allow us to manipulate both of our spin systems simultaneously. While we were able to detect signal in our high frequency system, we were unable to measure signal at our low frequency. We were unsuccessful in driving transitions at both frequencies simultaneously.

One of the difficulties in achieving a consistent result with our bimodal resonator stems from the relatively fragile structure of it. As discussed in section 5.2, the positioning of our two antennas relative to the resonator meant that our probes often ran into the resonator prongs. Each time that this happened and our prongs bent, the resonance changed slightly. Given the limited time, our solution to this was to implement a number of different dielectrics to increase stability without changing the resonance. We found that styrofoam worked the best given its relatively low dielectric constant due to it primarily being made of air. The issue was this is a very temporary solution, as the foam has limited rigidity to hold up to continued abuse of the resonator. Future trials should focus on finding a more consistent dielectric.

An alternative solution could be found by simulating and machining a resonator made out of something more durable and hard than copper. This

approach would have its own difficulties, with the machining process might be more difficult and the material changing our resonance and Q. A harder material would need more experimenting, but would potentially allow the resonator to hold form more consistently, leading to a more consistent resonance.

With an appropriate dielectric and probe set up, implementing the new bimodal resonator should allow DEER experiments to be run with relative ease. The work demonstrated in this thesis verifying that the behavior in each of the two spin systems is consistent with characteristics needed in qubits is encouraging. Future students focused on DEER experiments should be successful in measuring a coupling strength. Combining this work with the work done by [12] and [10] may allow the implementation of CNOT gates within a Cr_7Mn dimer system in the near future.

References

[1] Charles A. Collett and et al. A clock transition in the cr7mn molecular nanomagnet. *Magnetochemistry*, 5(1):4, January 2019.

[2] Grigore A. Timco, Eric J. L. McInnes, Floriana Tuna, and Richard E. P. Winpenny. Heterodimers of heterometallic rings. *Dalton Transactions*, 45(41):16610–16615, 2016.

[3] Charles A. Collett, Sofia M. Davvetas, and et al. An inexpensive, configurable two-tone electron spin resonance spectrometer. `https://doi.org/10.48550/arXiv.2407.21782`, 2024. Accessed: 2025-05-14.

[4] Wikipedia contributors. Spin echo. `https://en.wikipedia.org/wiki/Spin_echo`, January 2024. Accessed: 2025-05-14.

[5] Arzhang Ardavan, Alice M. Bowen, Antonio Fernandez, Alistair J. Fielding, Danielle Kaminski, Fabrizio Moro, Christopher A. Muryn, Matthew D. Wise, Albert Ruggi, Eric J. L. McInnes, Kay Severin, Grigore A. Timco, Christiane R. Timmel, Floriana Tuna, George F. S. Whitehead, and Richard E. P. Winpenny. Engineering coherent interactions in molecular nanomagnet dimers. *npj Quantum Information*, 1:15012, 2015.

[6] Josh Schneider and Ian Smalley. What is quantum computing? `https://www.ibm.com/topics/quantum-computing`, August 2024. Accessed: 2025-05-14.

[7] A Chiesa, P Santini, E Garlatti, F Luis, and S Carretta. Molecular nanomagnets: a viable path toward quantum information processing? *Reports on Progress in Physics*, 87(3):034501, feb 2024.

[8] Kai-Isaak Ellers. Enhancement of coherence times in the molecular nanomagnet cr7mn. Undergraduate thesis, Amherst College, 2019.

[9] Anthony Wilson, Muralee Murugesu, Wolfgang Wernsdorfer, Jonah J. Henderson, George Christou, and Stephen Hill. On the validity of the giant spin approximation and its application to single-molecule magnets. *Polyhedron*, 26(9–11):2065–2068, June 2007.

[10] Charles A. Collett, Paolo Santini, and et al. Constructing clock-transition-based two-qubit gates from dimers of molecular nanomagnets. *Physical Review Research*, 2(3):032037, August 2020.

[11] E. Garlatti and et al. A detailed study of the magnetism of chiral Cr7M rings: An investigation into parametrization and transferability of parameters. *Journal of the American Chemical Society*, 136:9763–9772, 2014.

[12] Rebecca Dalphin. Investigating faster quantum gate schemes for molecular nanomagnet qubits, December 2024.

[13] Gang Zhang and et al. Determining the hyperfine structure and clock transitions for kramers rare-earth ions in a crystal under a magnetic field: Beyond spin hamiltonian. *The Journal of Physical Chemistry C*, 126(23):9926–9936, June 2022.

[14] Matt A. Bernstein and et al. *Handbook of MRI Pulse Sequences*. Academic Press, 2004.

[15] George Rinard and Gareth Eaton. Loop-gap resonators. In *Biomedical EPR - Part B: Methodology, Instrumentation, and Dynamics*. Springer, Boston, MA, 2005.

[16] Jun Zhou and et al. Ultra-low mode volume on-substrate silicon nanobeam cavity. *Optics Express*, 27(21):30692, October 2019.

[17] Simon P. Neill and M. Reza Hashemi. In situ and remote methods for resource characterization. In *Fundamentals of Ocean Renewable Energy*, pages 157–191. Elsevier, 2018.

[18] Arzhang Ardavan, Olivier Rival, John J. L. Morton, Stephen J. Blundell, Alexei M. Tyryshkin, Gavin A. Timco, and Richard E. P. Winpenny. Will spin-relaxation times in molecular magnets permit quantum information processing? *Physical Review Letters*, 98(5):057201, January 2007.

[19] Pat Gumann and Jerry Chow. Ibm cools down world's largest quantum-ready cryostat: Ibm quantum computing blog. `https://www.ibm.com/quantum/blog/goldeneye-cryogenic-concept-system`, September 2022. Accessed: 2025-05-14.

[20] Peter P. Borbat and Jack H. Freed. Pulse dipolar electron spin resonance: Distance measurements. In Christine Belle and Gareth Eaton, editors, *Structural Information from Spin-Labels and Intrinsic Paramagnetic Centres in the Biosciences*, pages 1–38. Springer, 2013.

[21] Alexander Kenneth Axton. Preparing a sample probe for bimodal esr. Undergraduate thesis, Hamilton College, 2024.

[22] James Keeler. Coherence selection: Phase cycling and gradient pulses, 2000.

[23] Mark Tyestlin. Concept of phase cycling in pulsed magnetic resonance using sinusoidal magnetic field modulation. *Z Phys Chem*, 2016.

[24] COMSOL. Comsol multiphysics simulation software. `https://www.comsol.com/comsol-multiphysics`. Accessed: 2025-05-14.

[25] Mohammad-Reza Tofighi and et al. *Principles and Applications of RF/Microwave in Healthcare and Biosensing*. Elsevier/AP, Academic Press is an imprint of Elsevier, 2017.

A Design Drawings for Bimodal LGR